IAEA nuclear fusion

# Importance of $\delta B_{\parallel}$ on ETG stability, turbulence, and transport in NSTX

To cite this article: P.-Y. Li *et al* 2025 *Nucl. Fusion* **65** 106040

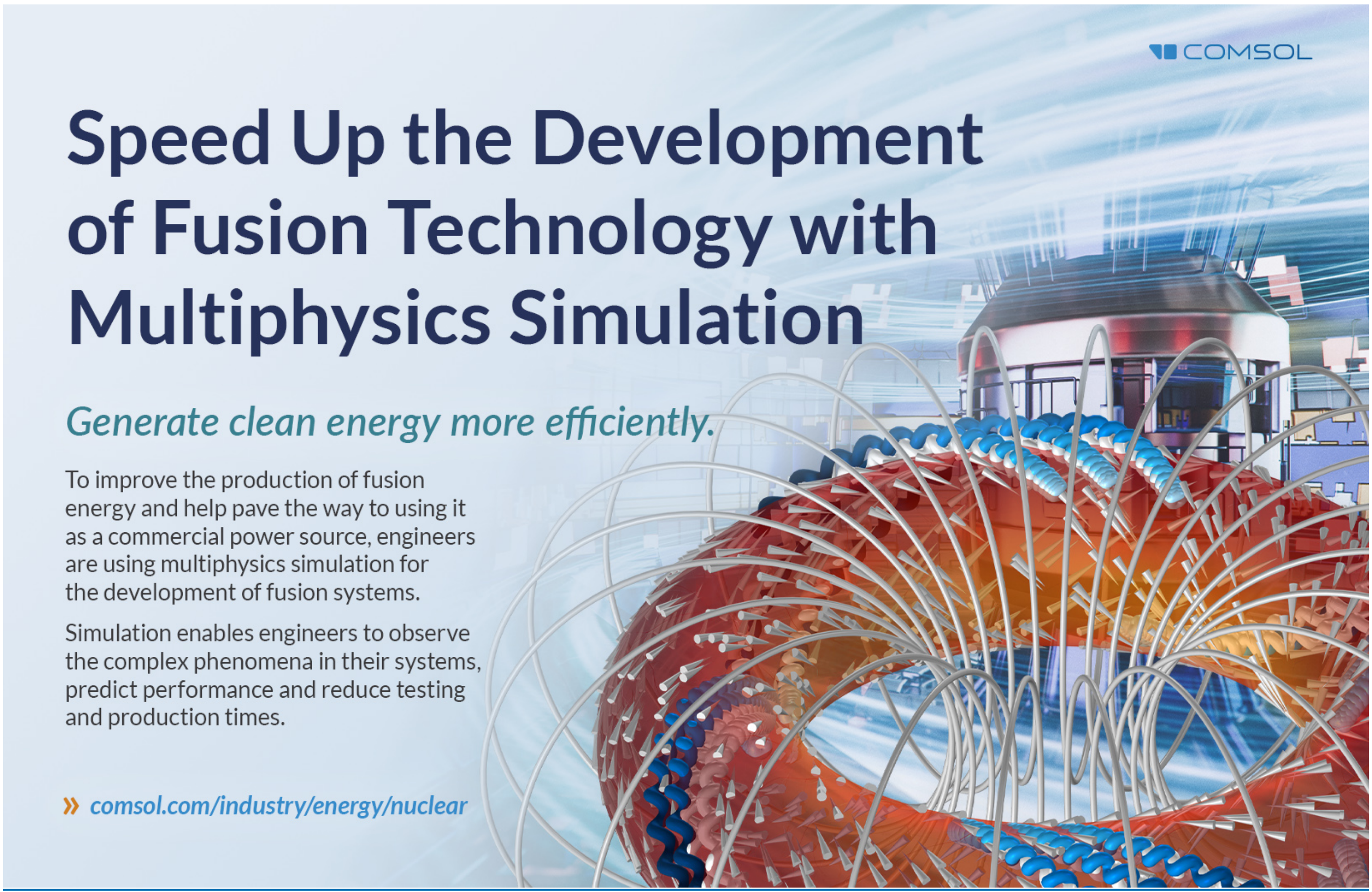

OPEN ACCESS
IOP Publishing | International Atomic Energy Agency
Nuclear Fusion
Nucl. Fusion 65 (2025) 106040 (20pp)
https://doi.org/10.1088/1741-4326/ae06b3

# Importance of $\delta B_{||}$ on ETG stability, turbulence, and transport in NSTX

**P.-Y. Li**[1,*], **D.R. Hatch**[1,2], **J.F. Parisi**[3], **M. Lampert**[3], **E.A. Belli**[4], **M. Kotschenreuther**[2] and **S.M. Mahajan**[1,2]

[1] Institution for Fusion Studies, The University of Texas at Austin, Austin, TX, United States of America
[2] ExoFusion, Austin, TX, United States of America
[3] Princeton Plasma Physics Laboratory, Princeton, NJ, United States of America
[4] General Atomics, San Diego, CA, United States of America

E-mail: pingyu.li@austin.utexas.edu

Received 24 April 2025, revised 23 August 2025
Accepted for publication 15 September 2025
Published 26 September 2025

**Abstract**

This study employs electron-scale gyrokinetic simulations to investigate the electron temperature gradient (ETG) driven instabilities, turbulence, and transport in the pedestal region of the National Spherical Torus Experiment, comparing non-lithiated (narrow pedestal) and lithiated (wide pedestal) scenarios. Our findings reveal that, in the non-lithiated case, a branch of strongly unstable ETG modes exhibiting finite parallel magnetic field fluctuations ($\delta B_{||} \neq 0$) emerges at the pedestal top and upper density pedestal region. This branch is uncovered only when $\delta B_{||}$ is retained in the simulations and is associated with substantial electrostatic electron heat flux. This region of strong ETG transport corresponds to the only region in the plasma where the pressure gradient is far below the critical gradient for kinetic ballooning modes. We investigated the origin of this finite $\delta B_{||}$ ETG branch by analyzing the gyrokinetic field equations. Nonlinear saturation is also analyzed and contrasted for simulations with and without $\delta B_{||}$. In contrast with the nonlithiated case, ETG modes in the lithiated case produce substantial transport in the steep gradient region, but are negligible at the pedestal top.

Keywords: ETG, NSTX, pedestal

(Some figures may appear in colour only in the online journal)

## 1. Introduction

A critical pursuit in fusion energy is to optimize plasma confinement enabled by edge transport barriers, particularly within the high confinement mode (H-mode) regime. The National Spherical Torus Experiment (NSTX) provides unique capabilities for exploring high confinement spherical tokamak scenarios. Notably, NSTX has explored both conventional scenarios with edge localized modes (ELMs) as well as unique scenarios exploiting lithium wall coatings to modify the conditions in the edge plasma. Lithiated discharges exhibit several appealing properties including (1) ELM-free operation and (2) wider, higher pedestals with correspondingly higher confinement [1–4].

In this work, the focus is on ETG transport at the top of the pedestal because of its unique physical drive mechanisms and its importance for electron thermal transport. This is an important contribution to a more comprehensive understanding of the transport dynamics that govern the pedestal evolution and pedestal structure in NSTX. Recent studies have applied gyrokinetic simulations to shed light on the influence of electron temperature gradient (ETG) turbulence on pedestal transport,

---

[*] Author to whom any correspondence should be addressed.

spanning conventional (e.g. JET, DIII-D) and spherical (e.g. MAST) tokamaks. [5–24]. In this paper, we describe CGYRO along with some GENE simulations [25, 26] of ETG transport in the NSTX pedestal, elucidating distinctive physical characteristics and comparing the dynamics in lithiated and nonlithiated discharges.

Transport mechanisms other than ETG have also been studied. Chowdhury *et a* [27] investigated microtearing modes (MTMs) at the pedestal top and their role in the electron heat flux. Dominski *et al* [28] studied MTMs across the pedestal for a lithiated NSTX shot, demonstrating good agreement between MTM frequencies and experimental measurements of magnetic fluctuations. Parisi *et al* [29] demonstrated that kinetic ballooning modes (KBMs) are a key constraint on pedestal width in the steep gradient region [30]

Our inquiry encompasses both narrow pedestal (nonlithiated, high recycling) and wide pedestal (lithiated, low recycling) configurations characterized by high triangularity. Notably, in the narrow pedestal scenario, parallel magnetic field fluctuations $\delta B_{||}$ emerge as a key component for ETG modes at larger electron scale wavenumbers in the density pedestal top and upper pedestal region. Nonlinearly, this results in substantial electrostatic electron heat flux. The importance of parallel magnetic fluctuations for ETG instabilities has been noted in [31] for NSTX with linear simulations and artificially enhanced normalized pressure gradient $\beta'$. Conversely, the wide-pedestal scenario showcases substantial transport in the steep-gradient region, but weak ETG modes in the pedestal top, suggesting that other transport mechanisms are likely dominant in setting pedestal profiles.

This paper is structured as follows: section 2 describes the activity of ETG turbulence based on local linear and nonlinear simulations within the narrow pedestal case across various radial locations encompassing the pedestal top and upper pedestal region. Additionally, simulations with parallel magnetic field fluctuations disabled in the pedestal top are conducted to underscore its pivotal role in ETG dynamics. The origins of the $\delta B_{||}$ effects are investigated by examination of the gyrokinetic field equations in various wavenumber limits. Analogous local simulations for the wide pedestal case are also presented in section 2.

## 2. ETG turbulence in a non-lithiated NSTX pedestal (shot 132 543)

The main focus of this work is ETG transport in the NSTX pedestal top, characterized by a large $\eta = L_{\mathrm{n}}/L_{\mathrm{T}}$, the ratio of density scale length $1/L_{\mathrm{n}} = (\mathrm{d}n/\mathrm{d}r)/n$ to temperature scale length $1/L_{\mathrm{T}} = (\mathrm{d}T/\mathrm{d}r)/T$. For the NSTX shot 132 543, $\eta$ is large because of weak density gradients at the pedestal top. As will be described below, ETG turbulence produces substantial transport in the pedestal top region, making it the likely mechanism that governs $T_{\mathrm{e}}$ profiles in the transition between the pedestal and the core in the narrow pedestal scenario. Moreover, the ETG turbulence, with substantial $\delta B_{||}$, has distinctive and novel electromagnetic characteristics. For these reasons, we focus largely on the pedestal top. On the other hand, ETG turbulence in the steep gradient region for shot 132 543 where both $1/L_{\mathrm{n}}$ and $1/L_{\mathrm{T}}$ are large has been investigated in [6] where the ETG heat flux can reach up to 1–2 MW. We carried out several simulations to reproduce those results but will not report them here. Note that the resolutions adopted can be found in appendix.

Figures 1 and 2 illustrate the three radial locations at $\rho_{\mathrm{tor}} = 0.862, 0.876, 0.890$, chosen to span the density pedestal top with large temperature gradients within the narrow pedestal scenario. Note that $\rho_{\mathrm{tor}} = \sqrt{\Phi_0/\Phi_{\mathrm{lcfs}}}$, where $\Phi_0$ is the toroidal flux in the center and $\Phi_{\mathrm{lcfs}}$ is the one for the last closed surface. In this figure, $f_p = (1/L_{\mathrm{n}}) / (1/L_{\mathrm{n}} + 1/L_{\mathrm{T}})$ [34] serves as a metric quantifying the fraction of free energy drive attributable to the density gradient, and $\rho_{\mathrm{tor}}$ represents the square root of the normalized toroidal flux. Table 1 outlines the main physical input parameters for the simulations: including normalized plasma pressure $\beta_{\mathrm{e,unit}} = 8\pi n_{\mathrm{e}} T_{\mathrm{e}} / B_{\mathrm{unit}}^2$, safety factor $q_0$, normalized magnetic shear $\hat{s} = \frac{r}{q}\frac{\mathrm{d}q}{\mathrm{d}r}$, reference magnetic field in Tesla $B_{\mathrm{unit}}$, reference temperature in keV $T_{\mathrm{e}}$, reference density in $10^{19}\,\mathrm{m}^{-3}$, and the ratio of ion gyroradius to minor radius $\rho^* = \rho_{\mathrm{i}}/a$; $a$ and $R$ denote the minor and major radii, respectively.

### 2.1 Gyrokinetic simulations in the pedestal top

Figure 3 shows the growth rate spectrum, growth rate $\gamma$ versus binormal wavenumber $k_y\rho_{\mathrm{s}}$ (abbreviated to $k_y$ in the following discussions), calculated at $\rho_{\mathrm{tor}} = 0.862$ with linear gyrokinetic initial value runs with and without parallel magnetic field fluctuations ($\delta B_{||}$ on and off). Here, $\rho_{\mathrm{s}}$ is the ion gyroradius and $c_{\mathrm{s}}$ is the ion sound speed. Note that ion-scale turbulence ($k_y\rho_{\mathrm{s}} < 1$) does exist; however, it is not presented in this paper as the primary focus is on electron-scale turbulence.

An intriguing observation stemming from figure 3 is the notable discrepancy in growth rates between the simulations with $\delta B_{||}$ activated and deactivated ($\rho_{\mathrm{tor}} = 0.862$). Traditionally, ETG turbulence in conventional tokamaks has been presumed to be insensitive to the (electro) magnetic part of fluctuations (particularly $\delta B_{||}$) associated with the mode. In sharp contrast are the findings presented here for NSTX-there is a substantial increase in growth rates when $\delta B_{||}$ is kept in the calculations. It is evident that some part of the free energy is coupled to the mode through $\delta B_{||}$, with $\max(|\delta B_{||}|)/\max(|\Phi|) \sim 10\%$, a non-negligible magnitude. Note that it was first observed in linear simulations of [31] that $\delta B_{||}$ has a non-negligible effect on ETG growth rates in NSTX.

Figure 4 depicts the temporal evolution of heat fluxes derived from local nonlinear gyrokinetic simulations conducted with and without $\delta B_{||}$, where the analytic formula for the heat flux $Q$ will be defined in section 2.0.2. These simulations incorporate $E \times B$ shear, with $k_{y\mathrm{min}}\rho_{\mathrm{s}}$ set to 2. At $\rho_{\mathrm{tor}} = 0.862$, the heat flux calculated in the presence of $\delta B_{||}$ amounts to 10.6 MW (equivalent to 243 gyrobohm heat flux

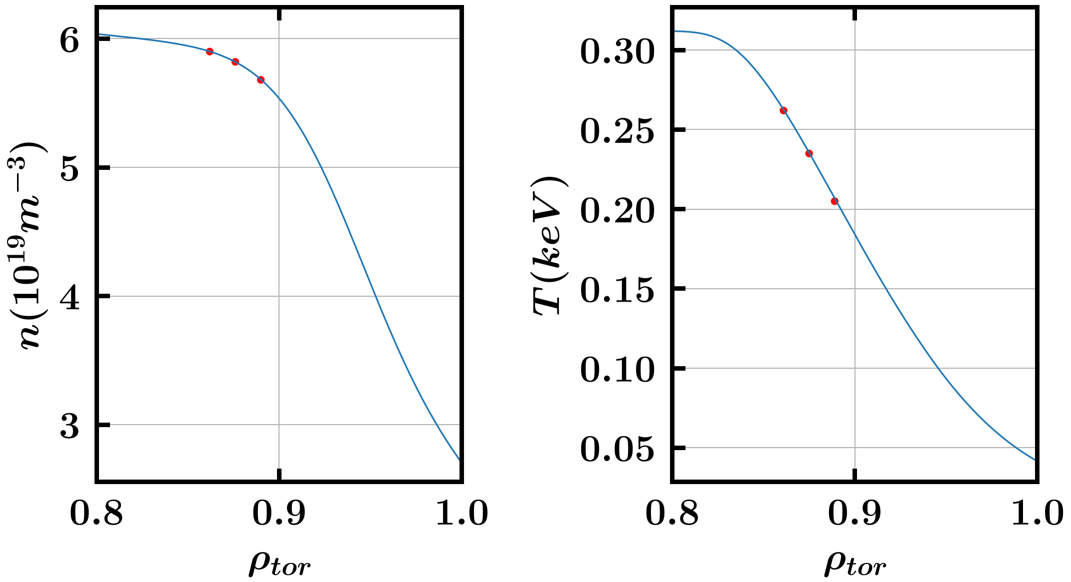

**Figure 1.** The electron density and temperature versus the square root of the normalized toroidal flux surface label $\rho_{\mathrm{tor}}$ for narrow pedestal case shot 132 543. The red dots represent the radial locations simulations are conducted.

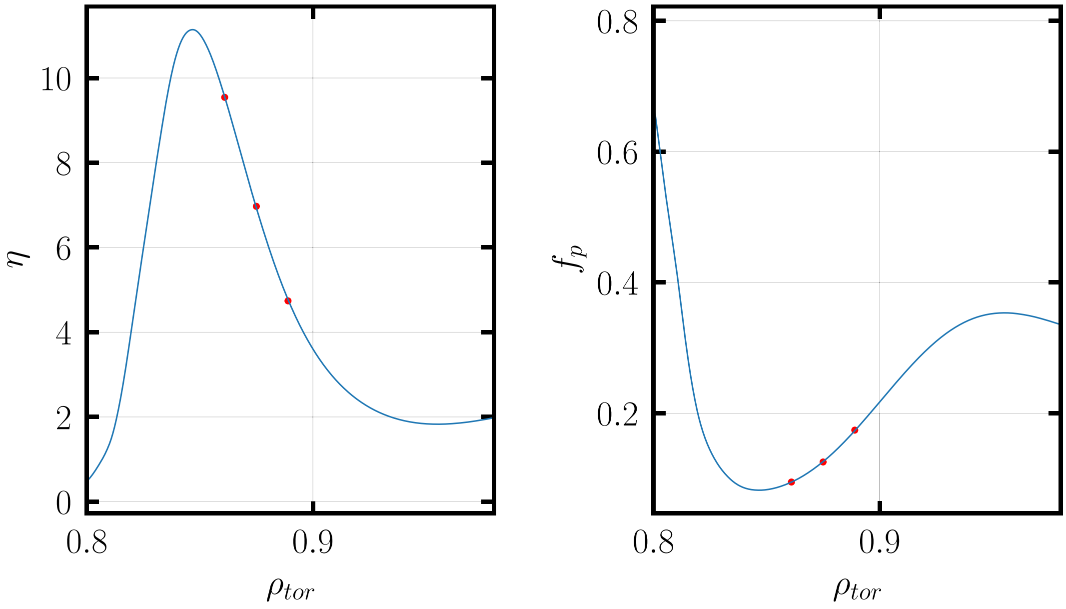

**Figure 2.** Radial profiles of $\eta$ and $f_{\mathrm{p}}$ for the narrow pedestal shot 132 543. $f_{\mathrm{p}}$ is used to quantify the portion of the pressure gradient contributed by the density gradient. For transport barrier geometries, the closer it is to 0.6, the less likely temperature-gradient-driven instabilities can access the free energy from temperature gradient [34].

**Table 1.** The physical parameters at $\rho_{\mathrm{tor}} = 0.862, 0.876, 0.890$ for shot 132 543 at 700 ms, respectively. $\eta$ and $\beta$ decrease as $\rho_{\mathrm{tor}}$ increases. Magnetic shear does not vary a lot around the pedestal top.

| $\rho_{\mathrm{tor}}$ | $q_0$ | $\hat{s}$ | $\omega_{\mathrm{ne}}$ | $\omega_{\mathrm{Te}}$ | $\eta$ | $\beta_{\mathrm{e,unit}}$ | $B_{\mathrm{unit}}(T)$ | $T_{\mathrm{e}}$(keV) | $n_{\mathrm{e}}(10^{19}m^{-3})$ | $\rho^*$ |
|---|---|---|---|---|---|---|---|---|---|---|
| 0.862 | 6.27 | 5.75 | 1.12 | 10.68 | 9.54 | 0.21% | 1.71 | 0.263 | 5.9 | 0.002 27 |
| 0.876 | 6.63 | 5.87 | 1.94 | 13.5 | 6.96 | 0.18% | 1.76 | 0.236 | 5.82 | 0.002 09 |
| 0.890 | 7.02 | 6.21 | 3.43 | 16.7 | 4.67 | 0.15% | 1.81 | 0.206 | 5.68 | 0.0019 |

$Q_{\mathrm{GB}}$), significantly exceeding the heat flux of 0.267 MW (6.16 $Q_{\mathrm{GB}}$) obtained without $\delta B_\parallel$. This discharge was heated by a total heating power of 6 MW, indicating that the former overestimates the heat flux, while the latter would suggest that ETG turbulence is negligible. Additionally, the scenario with $\delta B_\parallel$ active also has a modest negative electromagnetic

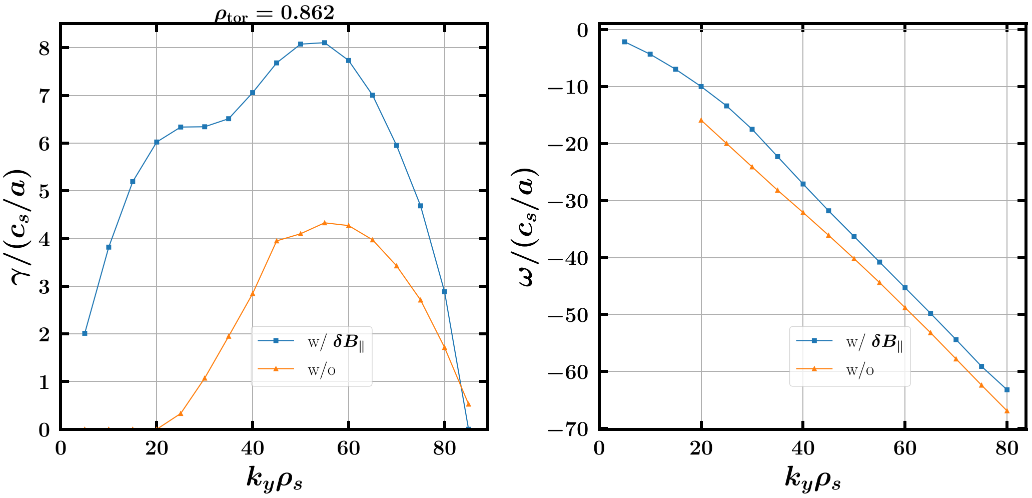

**Figure 3.** ETG modes growth rate spectrum comparison with and without $\delta B_\parallel$ for shot 132 543. The difference is the largest at $k_y = 20$ and reduces as the scale becomes smaller. Note that the type of mode resonance changes when going from larger to smaller scales, which will be discussed later in this section.

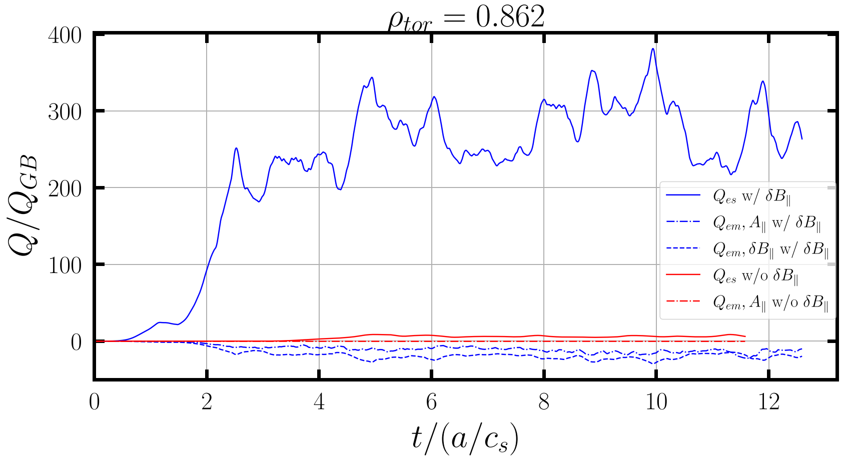

**Figure 4.** Electron heat flux comparisons with and without $\delta B_\parallel$ for shot 132 543 at $\rho_{\rm tor} = 0.862$. Turning on $\delta B_\parallel$ significantly increases the electrostatic heat flux $Q_{es}$ and also drives negative electromagnetic heat flux $Q_{\rm em}$. Note that $Q_{\rm em}$ contributed by $\delta B_\parallel$ is larger than the part contributed by $A_\parallel$. Also, the heating power is ∼6 MW, which is lower than 10.6 MW (243 $Q_{\rm GB}$), exceeding the heat flux of 0.267 MW (6.16 $Q_{\rm GB}$) obtained without $\delta B_\parallel$. Also note that the time is normalized to $a/c_{\rm s}$, which is an ion time scale, so the total simulation time is in fact several hundred electron time scales.

heat flux. Figure 5 shows the heat flux spectrum with and without $\delta B_\parallel$. Including $\delta B_\parallel$ leads to a significant increase in heat flux across the entire range, particularly at the larger electron scales, which is stable when $\delta B_\parallel$ is omitted. Note that although the growth rate peaks at $k_y \sim 50$ when $\delta B_\parallel$ is included, the peak heat flux is expected to occur at lower $k_y$ in the spectrum. This is because smaller-scale modes exhibit stronger nonlinear interactions, which can dominate unless the corresponding growth rates at higher $k_y$ are significantly larger.

It is also worth noting that the overestimation of the calculated heat flux with $\delta B_\parallel$ turned on could be attributed to several factors, including the stiffness of heat transport, global effects, or multi-scale interactions. These factors will be discussed in more depth below. Also, note that the numerical resolutions are presented in appendix.

#### *2.1.1. ETG transport and KBM limits.*

The strong transport from ETG in the pedestal top is interesting in the context of figure 6, which shows the experimental profile of $\alpha_{\rm MHD}$ for the NSTX shot 132 543 along with symbols denoting the KBM limit calculated from gyrokinetic simulations [32]. It is striking that the experimental profile closely corresponds to the KBM limit spanning almost the entire device. The only region where the experimental profile is substantially below the KBM limit (by roughly a factor of two at most) is the pedestal top region precisely where our analysis shows strong transport from electromagnetic ETG turbulence. This raises the question of whether the electromagnetic ETG turbulence is sufficiently strong to constrain the plasma below the KBM limit in this region. It remains an open question whether ETG turbulence could constrain the pressure

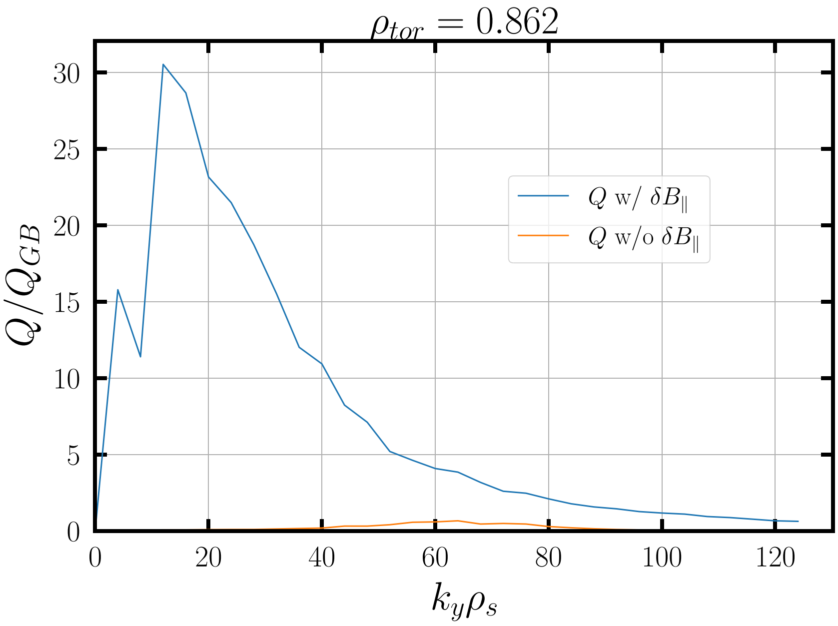

**Figure 5.** Electron heat flux spectrum comparisons with and without $\delta B_{\parallel}$ for shot 132 543 at $\rho_{\rm tor} = 0.862$. Turning on $\delta B_{\parallel}$ significantly increases the heat flux across the whole range especially in the larger electron scale.

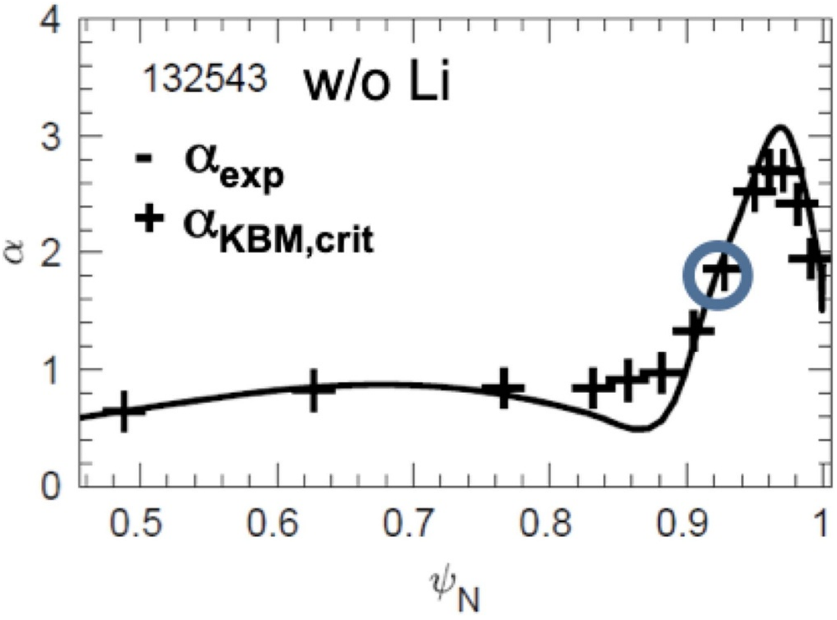

**Figure 6.** The KBM threshold for shot 132 543. $\psi_{\rm N}$ is the normalized poloidal flux. The $\alpha_{\rm exp}$ in the region $\psi_{\rm N} = 0.74 \sim 0.93$ ($\rho_{\rm tor} = 0.65 \sim 0.87$) is below the KBM limit. This corresponds to the region of high electromagnetic ETG transport. Reproduced with permission from [6].

profile in this region despite the fact that it produces predominantly electron thermal transport and small particle transport. Further investigation of this question would require additional information about the particle source and particle transport in this region, which is beyond the scope of this work.

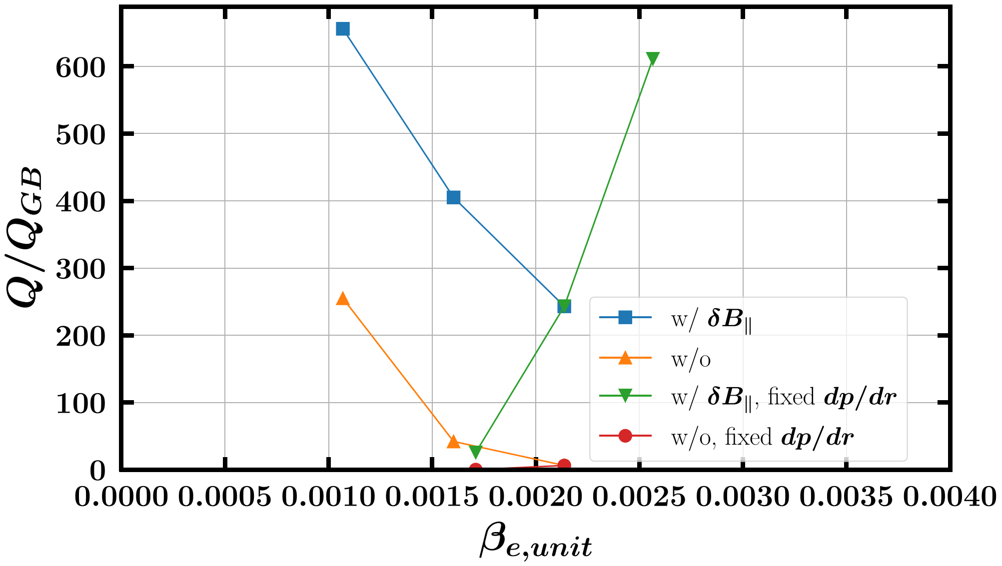

**Figure 7.** The heat flux produced by ETG turbulence reduces for both with and without $\delta B_\parallel$ when $\mathrm{d}p/\mathrm{d}r$ is not fixed as $\beta_{\mathrm{e,unit}}$ increases. The trend is completely opposite when $\mathrm{d}p/\mathrm{d}r$ is fixed.

#### 2.1.2. Electromagnetic effects on heat flux.

The heat flux $Q_j$ of species $j$ is defined as [40–44]

$$Q_j = \frac{n_{0j}T_{0j}}{\int_{-\pi}^{\pi} J\mathrm{d}z} \int_{-\pi}^{\pi} \mathrm{d}z \sum_k Jik_y \left[\pi B_0(z) \int \mathrm{d}v_\parallel \mathrm{d}\mu v^2 f^*_{j,k}\chi_k\right], \tag{1}$$

and normalized to the gyroBohm heat flux, $n_{\mathrm{ref}}T_{\mathrm{ref}}c_{\mathrm{ref}}\rho^2_{\mathrm{ref}}/L^2_{\mathrm{ref}}$, where $f_{j,k}$ is the total perturbed distribution function, $\chi_{j,k} = \bar{\Phi}_k - v_{Tj}v_\parallel \bar{A}_{\parallel,k} + \frac{T_{0j}}{q_j}\mu\delta\bar{B}_{\parallel,k}$ is the modified potential, $v_{Tj}$ is the species-dependent thermal velocity, $\bar{\Phi}_k$ is the gyroaveraged electric potential, $\bar{A}_{\parallel,k}$ is the gyroaveraged parallel magnetic vector potential, $v_\parallel$ is the parallel velocity, $\delta\bar{B}_{\parallel,k}$ is the gyroaveraged parallel magnetic field fluctuation, $n_{j0}$ is the background density, $T_{j0}$ is the background temperature, $q_j$ is the charge, $F_{j0}$ is the background Maxwellian, $\mathbf{v} = (v_\parallel, \mu)$ is the velocity vector, and $B_0(z)$ is the background magnetic field.

In figure 4, the contributions of $A_\parallel$ and $\delta B_\parallel$ to $Q_{\mathrm{em}}$ are observed to be negative, with $\delta B_\parallel$ contributing 50% more than $A_\parallel$. Conversely, the total $Q_{\mathrm{em}}$ amounts to approximately 20% of $Q_{\mathrm{es}}$, a significantly higher proportion compared to the scenario without $\delta B_\parallel$.

The impact of electromagnetic effects on the electrostatic heat flux, which depends only on the electrostatic potential, $\Phi$, changes significantly when $\delta B_\parallel$ is toggled on and off in simulations. This suggests that $\delta B_\parallel$ strongly influences $\Phi$ in the present case. To better understand the role of $\delta B_\parallel$, we adjust $\beta_{\mathrm{e,unit}}$ to examine how electromagnetic effects scale the heat flux.

Figure 7 shows the total heat flux $Q$ found in nonlinear gyrokinetic $\beta_{\mathrm{e,unit}}$ scans, comparing cases with and without $\delta B_\parallel$ and whether $\mathrm{d}p/\mathrm{d}r$ is fixed. Specifically, we consider two approaches: one where $\mathrm{d}p/\mathrm{d}r$ is self-consistently adapted along with $\beta$, maintaining equilibrium consistency, and another where $\mathrm{d}p/\mathrm{d}r$ is decoupled from $\beta$, allowing independent variation. In the self-consistent case, increasing $\beta$ leads to a corresponding increase in $\mathrm{d}p/\mathrm{d}r$, ensuring consistency with the equilibrium. Since $\mathrm{d}p/\mathrm{d}r$ is closely related to the MHD stability parameter $\alpha_{\mathrm{MHD}}$, which plays a central role in the equilibrium and magnetic geometry, this distinction is crucial for understanding the impact of electromagnetic effects on heat flux. Importantly, this increase in $\mathrm{d}p/\mathrm{d}r$ does not appear in the gradient scale lengths-such as the $\omega_*$ term-but instead manifests through $\alpha_{\mathrm{MHD}}$, which directly influences equilibrium and geometry.

As $\beta_{\mathrm{e,unit}}$ increases, the heat flux produced by ETG turbulence decreases for simulations both with and without $\delta B_\parallel$ when $\mathrm{d}p/\mathrm{d}r$ is adapted self-consistently (note that this is the most physically-relevant test of electromagnetic effects). In contrast, when $\mathrm{d}p/\mathrm{d}r$ is fixed, the trend is reversed. This suggests that increasing $\beta$ enhances the influence of $\delta B_\parallel$, while the pressure gradient contributes to ETG mode stabilization through its effect on the equilibrium geometry.

### 2.2. $\delta B_\parallel$ in the gyrokinetic field equations

To find out why $\delta B_\parallel$ can have such a great effect on ETG turbulence, we begin by asking two questions: (1) what makes $\delta B_\parallel$ large enough to play an important role and (2) how does $\delta B_\parallel$ affect ETG turbulence. In order to answer the first question, we first consider two possibilities: (i) that the effect originates from the direct impact of $\delta B_\parallel$ in the gyrokinetic equation, and (ii) that its impact arises from its coupling to $\Phi$ in the field equations.

We begin with the gyrokinetic equation for the perturbed distribution function $g_{j,k}$ (sometimes called the generalized distribution function) for species $j$ (see [33] for details and normalizations). Its evolution is governed by the gyrokinetic equation $\partial g_{j,k}/\partial t = L[g_{j,k}] + N[g_{j,k}]$, where $L$ and $N$ represent the linear and nonlinear operators, with

$$L\left[g_{j,k}\right] = -\omega_* F_{j0} i k_y \chi_{j,k} + \frac{\beta T_{j0}}{q_j B_0^2} v_\parallel^2 \omega_p \Gamma_{y,j,k} - \frac{v_{\mathrm{T}j}}{J B_0} v_\parallel \Gamma_{z,j,k}$$

$$- \frac{T_{j0}\left(2v_\parallel^2 + \mu B_0\right)}{q_j B_0}\left(K_y \Gamma_{y,j,k} + K_x \Gamma_{x,j,k}\right) + \frac{v_{\mathrm{T}j}}{2 J B_0} \mu \partial_z B_0 \frac{\partial f_{j,k}}{\partial v_\parallel}$$

$$+ \left\langle C_{j,k}\left(f\right)\right\rangle , \tag{2}$$

and

$$N\left[g_{j,k}\right] = \sum_{k'} \left(k_x' k_y - k_x k_y'\right) \chi_{j,k'} g_{j,k''} \ , \tag{3}$$

where $\mathbf{k}'' = \mathbf{k} - \mathbf{k}' = (k_x - k_x', k_y - k_y')$, $\omega_* = \omega_{\mathrm{n},j,k} + \left(v_\parallel^2 + \mu B_0 - 3/2\right)\omega_{\mathrm{T},j,k}$, while $f_{j,k} = g_{j,k} - \frac{2q_j}{m_j v_{\mathrm{T}j}} \bar{A}_{\parallel,k} F_{j0}$ is the total perturbed distribution function, $\omega_p = a/L_{\mathrm{p}}$ is the normalized pressure gradient, $K_{x,y}$ are the curvature terms, $\Gamma_{x,y} = i k_{x,y} g + \frac{q_j}{T_{j0}} F_{j0} i k_{x,y} \chi$, and $\Gamma_z = \partial_z g + \frac{q_j}{T_{j0}} F_{j0} \partial_z \chi + \frac{v_{\mathrm{T}j} q_j}{T_{j0}} v_\parallel \mu F_{j0} \bar{A}_{\parallel,k} \partial_z B_0$.

In light of the fact that ETG is an intrinsically electro static instability (i.e. it can exist in the purely electrostatic limit), one should look at how $\delta B_{\parallel,k}$ affects $\Phi_k$. It can be seen that $\delta B_{\parallel,k}$ enters the gyrokinetic equation solely through $\chi_{j,k} = \bar{\Phi}_k - v_{\mathrm{T}j} v_\parallel \bar{A}_{\parallel,k} + \frac{T_{0j}}{q_j} \mu \delta \bar{B}_{\parallel,k}$. Although the coefficients for $\Phi_k$ and $\delta B_{\parallel,k}$ have the same ordering according to standard gyrokinetic orderings, it remains unclear whether $\delta B_{\parallel,k}$ has a direct impact on $\Phi_k$. Hence, we turn to the perpendicular part of Faraday's law and the Poisson equation, which in fact couple $\Phi$ and $\delta \bar{B}_{\parallel,k}$ through gyromotions. We now begin the investigations on the normalized field equations,

$$\left(k_\perp^2 \lambda_{\mathrm{D}}^2 + \sum_j \frac{q_j^2}{T_{0j}} n_{0j}\left(1 - \Gamma_0\left(b_j\right)\right)\right)\Phi_k - \sum_j \frac{q_j n_{0j}}{B_0} \Delta\left(b_j\right) \delta B_{\parallel,k}$$

$$= \sum_j n_{0j} \pi q_j B_0 \int J_0\left(\lambda_j\right) g_{j,k} \mathrm{d}v_\parallel \mathrm{d}\mu \ , \tag{4}$$

$$-\sum_j \frac{q_j n_{0j}}{B_0} \Delta\left(b_j\right) \Phi_k + \left(\frac{2}{\beta} - \sum_j \frac{2 T_{0j} n_{0j}}{B_0^2} \Delta\left(b_j\right)\right) \delta B_{\parallel,k}$$

$$= \sum_j n_{0j} \frac{\pi v_{\mathrm{T}j} q_j B_0^{3/2}}{k_\perp} \int \sqrt{\mu} J_1\left(\lambda_j\right) g_{j,k} \mathrm{d}v_\parallel \mathrm{d}\mu \ , \tag{5}$$

where $b_j = \frac{T_{0j} m_j}{q_j^2 B_0^2} k_\perp^2$, $\lambda_j = \frac{v_{\mathrm{T}j}}{\Omega_j} k_\perp \sqrt{B_0 \mu}$, $\Gamma_n(x) = \mathrm{e}^{-x} I_n(x)$, $\Delta(x) = \Gamma_0 - \Gamma_1$, $I_n$ is the modified Bessel functions. The normalizations can be found in [40]. Note that the parallel part of Faraday's law that only includes $\bar{A}_{\parallel,k}$ and $g_{i,k}$ is not included in this discussion for $\delta \bar{B}_{\parallel,k}$. Now we start looking at the effect of $\delta B_\parallel$ in the long wavelength limit $k_\perp \rho_i$, $k_\perp \rho_{\mathrm{e}}$, $k_\perp^2 \lambda_{\mathrm{D}}^2 \ll 1$, where $\Gamma_0(b_j) = 1$, $\Gamma_1(b_j) = 0$, and $\Delta(b_j) = 1$. Note that this limit is not relevant for ETG instabilities, but we discuss it here for completeness. For simplicity, we will keep only two species, ions and electrons, with $n_{0\mathrm{i}} = n_{0\mathrm{e}} = n_0$. Since in this limit, $\sum_j \frac{q_j n_{0j}}{B_0} \Delta\left(b_j\right) = 0$, $\Phi$ drops out of equation (5) and $\delta B_{\parallel,k}$ drops out of the Poisson equation. Hence, equation (5) becomes the only equation involving $\delta B_{\parallel,k}$. Now the only way for $\delta B_\parallel$ to impact the dynamics is if $\beta$ become large enough so that $\delta B_{\parallel,k}$, which is proportional to $\beta$, can attain a sufficiently high amplitude to affect the dynamics solely through $\chi$ in the gyrokinetic equation. A more detailed discussion can be found in [37]. In contrast to this low-k limit, other mechanisms are required for ETG.

To see how $\delta B_\parallel$ affects ETG, we begin by looking at the intermediate regime where $k_\perp \rho_i \gg 1$, $k_\perp^2 \lambda_{\mathrm{D}}^2 \ll 1$, and no assumptions for $k_\perp \rho_{\mathrm{e}}$, which to the lowest order leads to $\Gamma_0(b_i) = 0$, $\Delta(b_i) = 0$. By adopting the convention for effective ion charge $Z_{\mathrm{eff}} = \sum_{\mathrm{i}} n_{\mathrm{i}} q_{\mathrm{i}}^2 / n_{\mathrm{e}}$ and $n_{0\mathrm{e}} = 1$, equations (4) and (5) then become

$$\left(\frac{Z_{\mathrm{eff}}}{T_{0\mathrm{i}}} + \frac{q_{\mathrm{e}}^2}{T_{0\mathrm{e}}}\left(1 - \Gamma_0\left(b_{\mathrm{e}}\right)\right)\right)\Phi_k - \frac{q_{\mathrm{e}}}{B_0} \Delta\left(b_{\mathrm{e}}\right) \delta B_{\parallel,k} = \pi q_{\mathrm{e}} B_0$$

$$\times \int J_0\left(\lambda_e\right) g_{\mathrm{e},k} \mathrm{d}v_\parallel \mathrm{d}\mu \ , \tag{6}$$

$$- \frac{q_{\mathrm{e}}}{B_0} \Delta\left(b_{\mathrm{e}}\right) \Phi_k + \left(\frac{2}{\beta} - \frac{2 T_{0\mathrm{e}}}{B_0^2} \Delta\left(b_{\mathrm{e}}\right)\right) \delta B_{\parallel,k} = \frac{\pi v_{T\mathrm{e}} q_{\mathrm{e}} B_0^{3/2}}{k_\perp}$$

$$\times \int \sqrt{\mu} J_1\left(\lambda_{\mathrm{e}}\right) g_{\mathrm{e},k} \mathrm{d}v_\parallel \mathrm{d}\mu \ . \tag{7}$$

If we further assume $k_\perp \rho_{\mathrm{e}} \ll 1$ (which still applies to the larger-scale ETG instabilities as seen, for example, in figure 3), $\Gamma_0(b_{\mathrm{e}}) = 1$, $\Delta(b_{\mathrm{e}}) = 1$, $J_0(\lambda_{\mathrm{e}}) = 1$, and $J_1(\lambda_{\mathrm{e}}) = \lambda_{\mathrm{e}}/2$, equations (6) and (7) will then become

$$\frac{Z_{\mathrm{eff}}}{T_{0\mathrm{i}}} \Phi_k - \frac{q_{\mathrm{e}}}{B_0} \delta B_{\parallel,k} = \pi q_{\mathrm{e}} B_0 \delta n_{\mathrm{e}} \ , \tag{8}$$

$$- \frac{q_{\mathrm{e}}}{B_0} \Phi_k + \left(\frac{2}{\beta} - \frac{2 T_{0\mathrm{e}}}{B_0^2}\right) \delta B_{\parallel,k} = \mathrm{sgn}\left(q_{\mathrm{e}}\right) \pi T_{0\mathrm{e}} B_0 \left\langle \mu \right\rangle_{\mathrm{e}} \delta n_{\mathrm{e}} \ . \tag{9}$$

where $\delta n_{\mathrm{e}} = \int g_{\mathrm{e},k} \mathrm{d}v_\parallel \mathrm{d}\mu$, $\left\langle \mu \right\rangle_{\mathrm{e}} = \left(\int \mu g_{\mathrm{e},k} \mathrm{d}v_\parallel \mathrm{d}\mu\right) / \left(\int g_{\mathrm{e},k} \mathrm{d}v_\parallel \mathrm{d}\mu\right) = \left(\int \mu g_{\mathrm{e},k} \mathrm{d}v_\parallel \mathrm{d}\mu\right) / \delta n_{\mathrm{e}}$is the average electron magnetic moment. In order to check whether the parallel magnetic field fluctuations can cause non-negligible effects to electrostatic waves, we can look at the quantity $\delta B_{\parallel,k}/\Phi$ and adopt the conventions $q_{\mathrm{e}} = -q_{\mathrm{i}}$, $q_{\mathrm{i}} = 1$, $T_{0\mathrm{e}} = 1$, and $\tau = Z_{\mathrm{eff}} T_{0\mathrm{e}} / T_{0\mathrm{i}}$. In the pedestal region where we can assume small $\beta$, the ratio therefore can be expressed as

$$\frac{\delta B_{\parallel,k}}{\Phi_k} = \frac{\beta}{2}\left(\tau \left\langle \mu \right\rangle_{\mathrm{e}} - \frac{1}{B_0\left(z\right)}\right). \tag{10}$$

The ratio increases as $\beta$ increases in the low $\beta$ regime, which is not surprising since it is an electromagnetic fluctuation. Beside $\beta$, the more interesting part is how $\left\langle \mu \right\rangle_{\mathrm{e}}$, $B_0$, and $\tau$ affect the electromagnetic effects.

In equation (10), it becomes evident that the ratio increases with the rise in average electron magnetic moment $\langle\mu\rangle_e$ if $\langle\mu\rangle_e$ and $\tau$ are sufficiently large. Modes characterized by large $\langle\mu\rangle_e$ are typically associated with toroidal modes featuring the magnetic drift resonance, grad-B drift in particular, which are strongest within a narrow range of ballooning angles (small $k_x$) where the curvature is unfavorable. Note that in the steep gradient region, the dominant resonances are slab-like, meaning they primarily interact with $\langle v_\parallel\rangle$ rather than $\langle\mu\rangle$, which suppresses mechanisms that generate high $\langle\mu\rangle$ [38]. Additionally, $\beta$ is lower in this region, reducing the impact of magnetic fluctuations. This is consistent with the scenario described above for NSTX, wherein the parallel magnetic fluctuations are important at the pedestal top where the instabilities are more susceptible to toroidal resonances (due to weaker gradients) and $\beta$ is larger.

Beside understanding what makes $\delta B_{\parallel,k}$ large enough to be relevant, how $\delta B_{\parallel,k}$ affects ETG turbulence is still unanswered. Now we can consider the standard linearized gyrokinetic equation, with adiabatic and non-adiabatic particle responses treated separately:

$$\omega h_j + i v_\parallel \cdot \nabla h_j + i v_d \cdot \nabla h_j - i\langle C_j(f)\rangle = (\omega - \omega_{*j})\frac{q_j \bar{\chi}_j F_{j0}}{T_j}, \tag{11}$$

where $h_j = q_j \Phi F_{j0}/T_j + f_j$ represents the non-adiabatic response for specie $j$, $F_{j0}$ the Maxwellian distribution function, $v_d$ denotes the drift velocity operator arising from curvature and $\nabla B$. Expressed in Fourier space, this equation takes the form

$$h_j = \frac{\omega - \omega_{*j}}{\omega - \omega_d - v_\parallel k_\parallel - i\langle C_j(f)\rangle}\frac{q\bar{\chi}_{j,k}F_{j0}}{T_j}, \tag{12}$$

where $\omega_d$ is the drift frequency operator, and $k_\parallel$ denotes the parallel wavenumber operator.

As demonstrated in [39], in the collisionless limit, the field equations are complex symmetric. Consequently, the left eigenfunctions associated with $\Phi_k$, $A_{\parallel,k}$, and $\delta B_{\parallel,k}$ are given by $\Phi_k^*$, $A_{\parallel,k}^*$, and $\delta B_{\parallel,k}^*$, respectively. Given that electron-scale turbulence evolves on a timescale much faster than that of collisions, the collision operator can be neglected. Substituting equation (12) into the Poisson equation, integrating over $z$, and multiplying by the left eigenfunction $(\Phi_k^*)^*$ while neglecting the non-adiabatic ion response for electron-scale turbulence and assume a low-$\beta$ regime, allowing higher-order terms to be dropped, we obtain

$$\frac{Z_{\mathrm{eff}}}{T_i} + \frac{1}{T_e} - \frac{1}{T_e}\int d^3v \frac{\omega - \omega_{*e}}{\omega - \langle\omega_d\rangle - v_\parallel\langle k_\parallel\rangle}\frac{qF_{e0}}{T_e} = 0, \tag{13}$$

where $Z_{\mathrm{eff}} = \sum_i n_i q_i^2/n_e$ is the effective ion charge, and the averaged drift frequency and parallel wavenumber are defined as

$$\langle\omega_d\rangle = \frac{\int \Phi_k \omega_d \bar{\chi}_{e,k} dz}{\int \Phi_k \Phi_k dz}, \quad \langle k_\parallel\rangle = \frac{\int \Phi_k k_\parallel \bar{\chi}_{e,k} dz}{\int \Phi_k \Phi_k dz}. \tag{14}$$

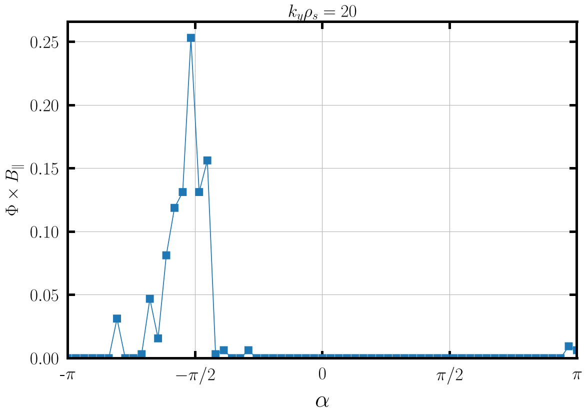

**Figure 8.** Cross phase histogram between $\Phi_k$ and $\delta B_{|,k}$ of a linear run for $k_y = 20$ in shot 132 543 at $\rho_{\mathrm{tor}} = 0.862$. The near $\pi/2$ phase shift suggests that $\delta B_{|,k}$ plays an important role in ETG turbulence destabilization.

Equation (10) shows that the electron-weighted magnetic moment, $\langle\mu\rangle_e$, is inherently complex in $k$-space. This implies that $\delta B_{\parallel,k}$ and $\Phi_k$ can exhibit a phase difference, leading to additional imaginary components in $\langle\omega_d\rangle$ and $\langle k_\parallel\rangle$ due to the presence of $\delta B_{\parallel,k}$ in $\chi_{e,k}$. Consequently, the pole of the dispersion relation, dictated by the denominator, may shift in the complex plane, thereby altering the growth rate.

Figure 8 illustrates the cross-phase $\alpha$ histogram between $\Phi_k$ and $\delta B_{\parallel,k}$ of a linear run for $k_y = 20$ in shot 132 543 at $\rho_{\mathrm{tor}} = 0.862$, where $\alpha(t) = \arg\left(\langle\Phi^*(x,z,t)\,\delta B_\parallel(x,z,t)\rangle_{x,z}\right)$. The observed $\pi/2$ phase shift suggests that $\delta B_{\parallel,k}$ has a destabilizing influence on ETG turbulence.

An important consideration is whether alternative trial functions could be employed in the integral instead of the left eigenfunction. While integrating the Poisson equation with a different trial function yields another weak form of the gyrokinetic equation, the intrinsic properties of the system remain unchanged. However, in such cases, $\langle\omega_d\rangle$ and $\langle k_\parallel\rangle$ may become less well-defined due to the non-orthogonality of the eigenvectors. A more rigorous discussion of this issue is beyond the scope of this paper and will be explored in future work.

### 2.2.1. Testing $\mu$ resonance.

Figure 9 shows the growth rates plotted against ballooning angle for $k_y = 20$ and 50, both with and without the presence of $\delta B_\parallel$. Notably, the rapid decline in growth rates with increasing ballooning angles suggests the possibility of toroidal modes dominance. Note that in comparison to cyclone-base-case like geometry with ETG swapped with ion temperature gradient, the growth rates of ETG for $k_y = 20$ die out around $\theta/\pi \sim 0.5$, which is far larger than the case shown here (not shown to keep the discussion focused). It is important to note that equations (8) and (9) assume $k_\perp\rho_e \ll 1$, which holds true only when $k_x\rho_e$ is also significantly less than unity. However, for large $k_x$ values, $\Delta(b_e) \sim J_0^2$ promptly

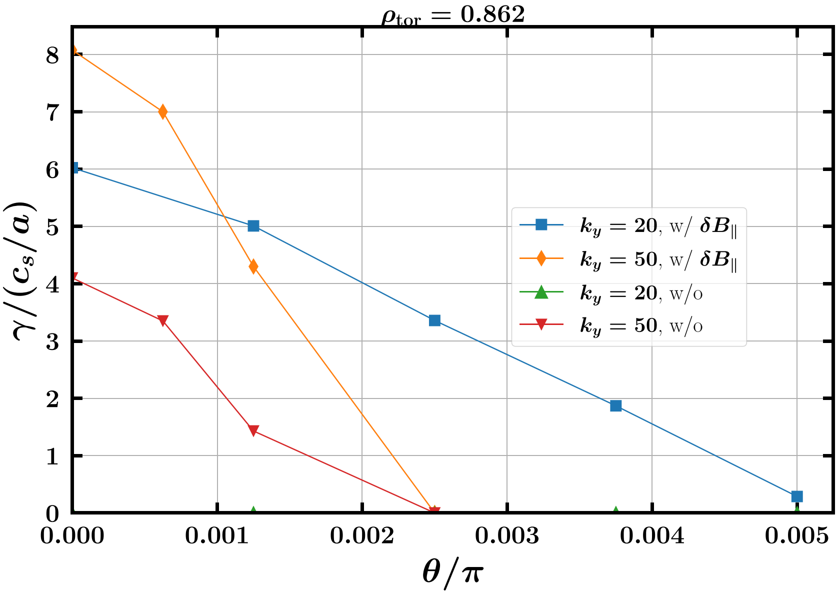

**Figure 9.** Growth rate versus ballooning angle for $k_y = 20$ and 50 for shot 132 543 at $\rho_{\rm tor} = 0.862$. Both with and without the presence of $\delta B_{\|}$. Notably, the rapid decline in growth rates with decreasing ballooning angles might be the result of toroidal mode dominance. No unstable mode is observed for $k_y = 20$ without $\delta B_{\|}$ across the ballooning angle.

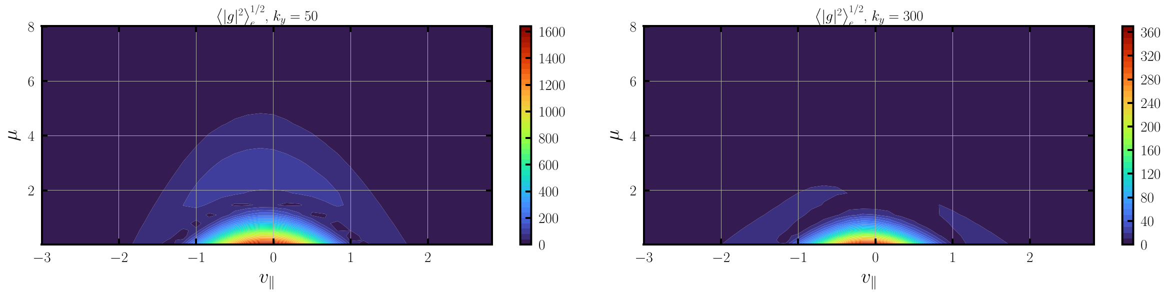

(a)

(b)

**Figure 10.** The velocity space contour plots of the distribution function $g$ in the outboard mid-plane for $k_y^{\rm GENE} = 50$ and $k_y^{\rm GENE} = 300$ for shot 132 543 at $\rho_{\rm tor} = 0.862$. The figures show there are stronger $\mu$ resonance (toroidal mode) for lower $k_y$ mode while the high $k_y$ mode has a stronger $v_{\|}$ resonance. Implying the $\delta B_{\|}$ effect will be more pronounce for the lower $k_y$ mode.

diminishes due to the finite-Larmor-radius effect, resulting in the decoupling of $\Phi$ and $\delta B_{\|}$. Consequently, the impact of $\delta B_{\|}$ on electrostatic waves becomes more pronounced for low $k_x$ modes. One may also wonder how modes confined to such a narrow range of ballooning angles can persist in nonlinear simulations. This is made possible by the combination of strong magnetic shear ($\hat{s} \sim 6$) and weak $E \times B$ shear ($\gamma_{E\times B} \sim 0.1$), a Floquet period argument suggests that the electron-scale turbulence-with its large linear growth rate ($\sim$8)-can survive despite the shearing effect.

The analytical result, that it is the $\mu$ resonance that boosts the growth rate so effectively through $\delta B_{\|}$, is confirmed by examining the distribution function directly in velocity space. It is apparent from figures 10(*a*) and (*b*) that the $k_y^{\rm GENE} = 50$ mode has a much stronger $\mu$ resonance compared to mode with $k_y^{\rm GENE} = 300$. This can be seen from the light blue regions in these figures: for the low $k_y$ mode, the band extends to high $\mu$, whereas for the high $k_y$ mode, the high $\mu$ region is depleted (dark) while the high $v_{||}$ regions are active. Based on equation (10), which represents the intermediate scale between ion and electron scales, and combined with the fact that $Z_{\rm eff}$ shown here is 2.77, the effect from $\delta B_{\|}$ should be pronounced for $k_y^{\rm GENE} = 50$ mode. It will be shown later in the subsection why the mode at $k_y^{\rm GENE} = 300$ shows little $\mu$ resonance and cares less about $\delta B_{\|}$. Note that the contour plots are derived from GENE [26], another widely used gyrokinetic codes, which has been extensively benchmarked with CGYRO for pedestal ETG modes [46]. Also, $B_{\rm ref}$ used in GENE is smaller than $B_{\rm unit}$ used in CGYRO, therefore, $k_y^{\rm GENE} = 300$ in GENE shown in figure 10(*b*) is $\sim$80 in CGYRO.

With the strong $\mu$ resonance, it is also apparent that finite-Larmor-radius effects will be important for large $k_x$ modes due

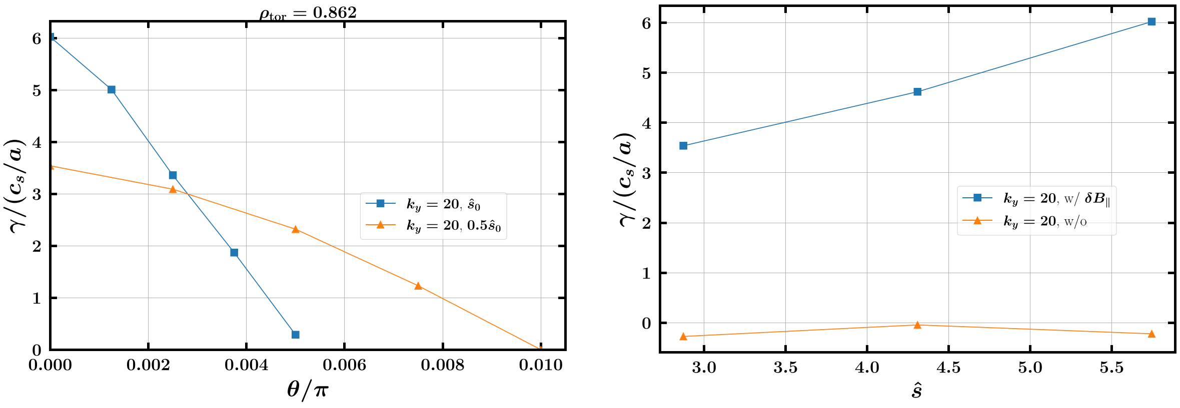

(a) (b)

**Figure 11.** (*a*) The growth rate spectrum for ballooning angle scan with different $\hat{s} = \hat{s}_0$ and $0.5\hat{s}_0$ at $k_y = 20$. Reducing $\hat{s}$ widens the ballooning angle growth rate spectrum and reduces the growth rate of the most unstable mode. (*b*) The growth rate spectrum for $\hat{s}$ scan at $k_y = 20$ with and without $\delta B_\parallel$. The difference between the growth rates for two cases with and without $\delta B_\parallel$ increases as $\hat{s}$ increases. Note that the plots are for shot 132 543 at $\rho_{\rm tor} = 0.862$.

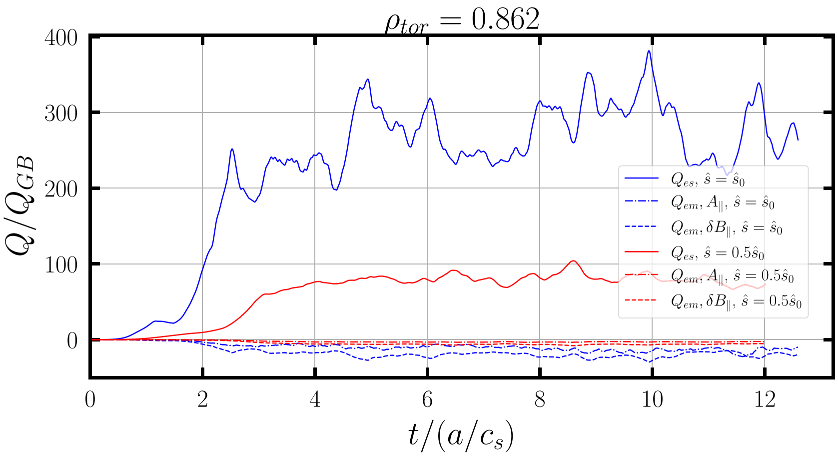

**Figure 12.** Heat fluxes time histories for shot 132 543 at $\rho_{\rm tor} = 0.862$. Heat flux is lowered 70% by cutting $\hat{s}$ by half while the electomagnetic heat flux also almost disappears. This suggests the large $\hat{s}$ is part of the reason why $\delta B_\parallel$ effect is so large.

to the Bessel function $J_0(k_\perp v_\perp/\Omega)$'s dependence on perpendicular velocity, which agrees with the result shown in figure 9.

The reason why ETG turbulence is so strongly ballooned in the outboard-midplane can be partially attributed to high magnetic shear $\hat{s}$. Figure 11(*a*) shows ballooning angle scans for the nominal magnetic shear from the experimental equilibrium, $\hat{s}_0$, as well as half that value: $0.5\hat{s}_0$. Figure 11(*b*) shows the growth rates versus $\hat{s}$ with and without $\delta B_\parallel$. The difference between the growth rates decreases as expected as $\hat{s}$ decreases. On the other hand, figure 12 shows the heat flux being lowered about 70% by cutting $\hat{s}$ by half. The electomagnetic heat flux also almost disappears because of the reduced $\hat{s}$. This implies the large $\hat{s}$ is part of the reason why $\delta B_\parallel$ effect is significant: higher $\hat{s}$ constrains the eigenmodes to the low $k_x$ regions where $\delta B_\parallel$ effects are more important.

By combining the results from equations (8)–(10), we deduce that the magnetic part of ETG($\delta B_\parallel$) has a pronounced effect on ETG growth at relatively large radial scales in the range determined by the ion and electron scales. This influence becomes particularly pronounced in scenarios with elevated $\beta$, as expected. The magnetic geometry of NSTX, with notably large magnetic shear $\hat{s}$, delineates a specific regime where ETG modes are compelled to reside at large radial scales. This localization places them in close proximity to regions in which $\delta B_\parallel$ is a major determinant of the mode dynamics. A detailed investigation on how magnetic geometry affects $\delta B_\parallel$'s impact on ETG turbulence in general cases is beyond the scope of this paper and is left for future research.

### 2.2.2. *Effect of $Z_{\rm eff}$ and temperature ratio on $\delta B_\parallel$.*

Beyond magnetic field considerations, the temperature ratio times the effective charge $\tau = Z_{\rm eff}T_{\rm e}/T_{\rm i}$ emerges as a crucial determinant of ETG mode behavior. While it is well-established that variations in $Z_{\rm eff}$, $T_{\rm e}$ and $T_{\rm i}$ can significantly modulate velocity space distributions and mode structures, making $\langle\mu_{\rm e}\rangle$ a function of the temperatures, equation (10) still suggests a correlation between $\tau$ and the $\delta B_\parallel$ effect. Specifically, an increase in $T_{\rm i}$, or a reduction in $\tau$, is anticipated to mitigate the influence of $\delta B_\parallel$.

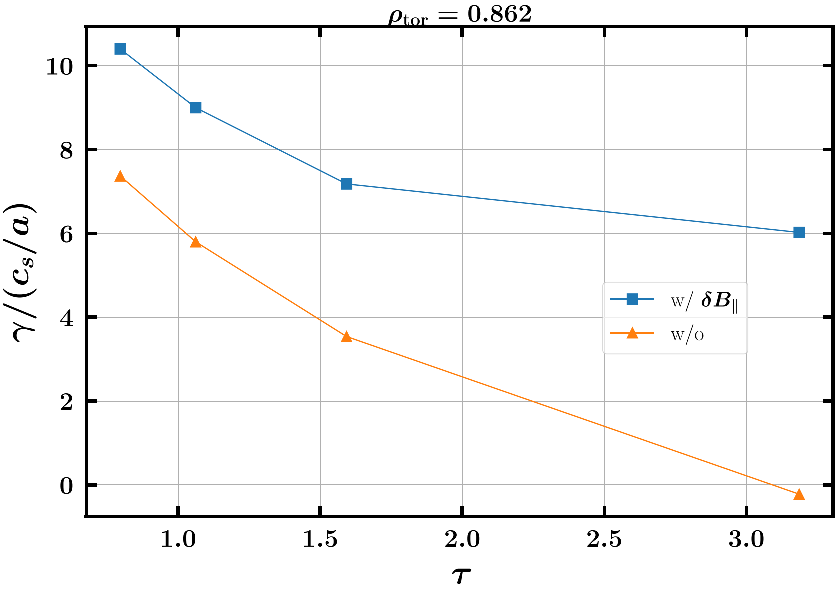

**Figure 13.** The growth rate versus $\tau = Z_{\rm eff}T_{\rm e}/T_{\rm i}$ for linear runs of shot 132 543 at $\rho_{\rm tor} = 0.862$. The difference between the growth rates with and without $\delta B_{\|}$ increases as $\tau$ increases, agreeing to equation (10).

To further elucidate these findings, figure 13 shows an ETG growth rate scan at $k_y = 20$ across a range of $\tau$ values by varying the ion temperature for a fixed electron temperature. As expected, the gap between the growth rates with and without $\delta B_{\|}$ increases as $\tau$ increases. Since $\tau = Z_{\rm eff}T_{\rm e}/T_{\rm i}$ is the factor that originates from the Poisson equation that enters the dispersion relation representing the ratio of the relative adiabaticity of the ions $(Z_{\rm eff}/T_{\rm i})$ and the electrons $(1/T_{\rm e})$. Lower ion temperature suggests ions are less adiabatic, therefore, less likely to counter the electromagnetic effects induced by electrons, including $\delta B_{\|}$.

Finally, we can look at the small-scale regime where $k_\perp\rho_i, k_\perp\rho_{\rm e} \gg 1$ but $k_\perp^2\lambda_{\rm D}^2$ is still not far larger than unity, of which the lowest order leads to $\Gamma_0(b_{\rm i}) = 0$, $\Delta(b_{\rm i}) = 0$, and $\Delta(b_{\rm e}) = 0$. Equations (4) and (5) can simply be reduced to

$$\Phi_k = \frac{\sum_j n_{0j}\pi q_j B_0 \int J_0(\lambda_j)\, g_{j,k} \mathrm{d}v_{\|}\mathrm{d}\mu}{\left(k_\perp^2\lambda_{\rm D}^2 + \frac{Z_{\rm eff}}{T_{0\rm i}} n_{0\rm e} + \frac{q_{\rm e}^2}{T_{0\rm e}}\left(1-\Gamma_0(b_{\rm e})\right) n_{0\rm e}\right)}\,, \tag{15}$$

$$\delta B_{\|,k} = \frac{\beta}{2}\sum_j n_{0j}\frac{\pi v_{Tj} q_j B_0^{3/2}}{k_\perp}\int \sqrt{\mu} J_1(\lambda_j)\, g_{j,k}\mathrm{d}v_{\|}\mathrm{d}\mu\,, \tag{16}$$

The vanishingly small value of the square of Debye length, denoted as $\lambda_{\rm D}^2 \sim 6.5\times10^{-6}\rho_{\rm s}^2$, plays a negligible role in the denominator within the observed unstable range. Consequently, the parameter $k_\perp^2\lambda_{\rm D}^2$ does not exert significant influence in our scenario. Instead, our analysis reveals that the ratio $\Phi_k/\delta B_{\|,k}$ scales proportionally to $\beta/k_\perp$. This outcome stems from the fact that the Bessel functions $J_0/J_1$ tend to approximately unity for large arguments, consistent with our findings in figures 3, 10(*b*), 14 and 15 where the disparities diminish notably at high $k_\perp$.

### 2.3. *ETG turbulence across the upper pedestal region*

Having examined a single radial position in great depth, we now broaden the investigation to additional radial points in the non-lithiated discharge further into the pedestal region (recall figure 2). The effects of $\delta B_{\|}$ persistently influence ETG turbulence dynamics. Figures 14 and 15 depict growth rate spectra that exhibit trends similar to those observed at $\rho_{\rm tor} = 0.862$. However, the disparity in growth rate spectra, both with and without $\delta B_{\|}$, is reduced for cases corresponding to $\rho_{\rm tor} = 0.876$ and $\rho_{\rm tor} = 0.890$.

If we look at the heat fluxes calculated from the nonlinear runs shown in figures 16 and 17, the difference between the heat fluxes with and without $\delta B_{\|}$ is still significant but smaller, where heat flux increases from $22Q_{\rm GB}$ to $252Q_{\rm GB}$ at $\rho_{\rm tor} = 0.876$ and $25Q_{\rm GB}$ to $251Q_{\rm GB}$ at $\rho_{\rm tor} = 0.890$.

In our analysis, it is apparent that $\delta B_{\|}$ exhibits a preference for impacting low $k_x$ modes, however, factors such as the local magnetic geometry and gradients do not force ETG modes as strongly at these two radial locations to live in small $k_x$ regimes. As illustrated in figure 18, the correlation length decreases with radial distance, suggesting that ETG turbulence experiences a weaker toroidal resonance and becomes more slab-like, extending to higher $k_x$ regions. This phenomenon might be the result of stronger $E\times B$ shear, which can break large scale modes into smaller eddies. It could also be that this partly arises from the heightened density gradient nearer to the plasma edge. In the study by Kotschenreuther *et al* [34], it is shown analytically that increased density gradients can compel temperature-gradient-driven modes to reside in larger $k_x$ regimes, diverging from the regions favored by $\delta B_{\|}$. Consequently, the influence of $\delta B_{\|}$ on ETG turbulence can be weakened as one moves away from regions with vanishingly

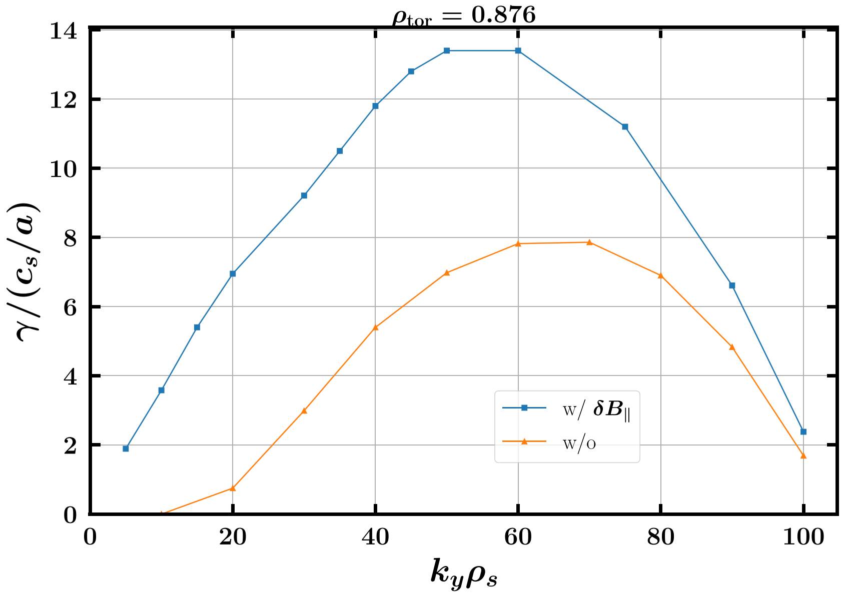

**Figure 14.** ETG modes growth rate spectrum comparison with and without $\delta B_{\|}$ for shot 132 543 at $\rho_{\rm tor} = 0.876$. Similar to figure 3, the difference is the largest in the range $k_y\rho_{\rm s} \ll 1 \ll k_y\rho_{\rm e}$.

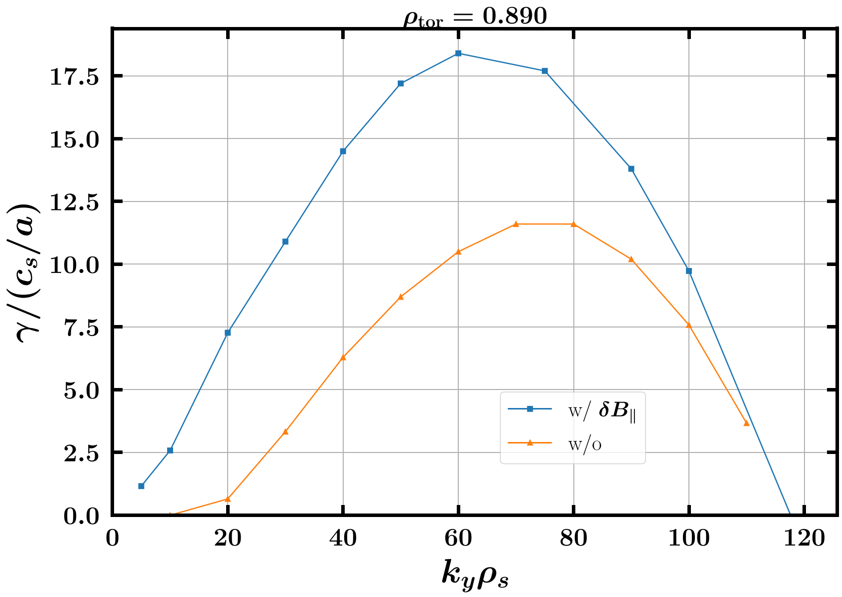

**Figure 15.** ETG modes growth rate spectrum comparison with and without $\delta B_{\|}$ for shot 132 543 at $\rho_{\rm tor} = 0.890$. Similar to figure 3, the difference is largest in the range $k_y\rho_{\rm s} \ll 1 \ll k_y\rho_{\rm e}$. The difference is also smaller than shown in figure 14.

small density gradients towards areas with steep gradients for the wide pedestal scenario.

## 3. ETG turbulence in a lithiated NSTX pedestal (shot 132 588)

We now turn our attention to ETG turbulence in a lithiated wide pedestal of shot 132 588 for which the profiles are plotted in figures 19; the red dots denote the simulated locations. Notably, the normalized ETG ($\eta = L_n/L_T$) is predominantly large only in the deep core of the device and the steep gradient region of the pedestal as shown in table 2 and figure 20. Extensive investigations, incorporating both linear and nonlinear simulations, confirm the absence or near absence of ETG turbulence in the density pedestal top ($\rho_{\rm tor} = 0.5$ and 0.55), regardless of whether $\delta B_{\|}$ is on or off.

Several factors contribute to the low level of ETG turbulence in these regions. Despite the large values of $\eta$, a key driver of ETG turbulence, the (normalized) ETG $\omega_{\rm Te}$ remains below unity for the investigated radial locations. This suggests that the gyrokinetic drive term for species $j$, denoted as $\omega_{*,j} = \omega_{{\rm n},j} + \left(v^2\| + \mu B_0 - 3/2\right)\omega_{{\rm T},j}$, is comparatively small in relation to other drift terms. Consequently, accessing free energy from temperature gradients becomes a challenge for ETG turbulence in these regions.

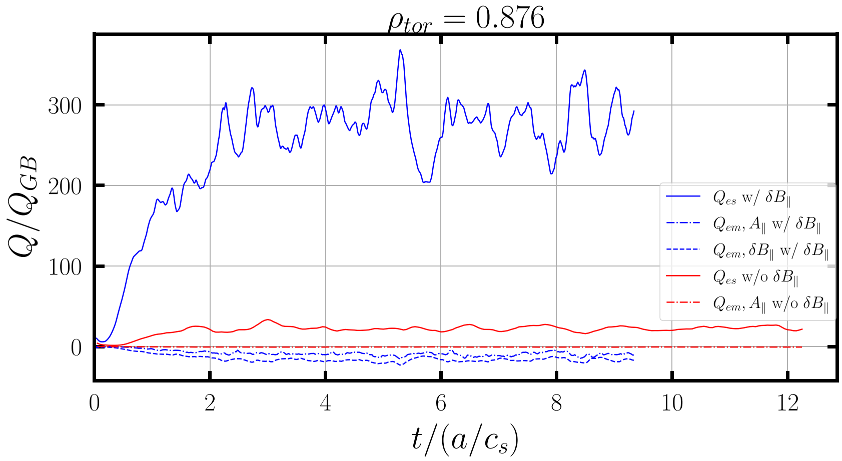

**Figure 16.** Heat flux comparisons with and without $\delta B_\parallel$ for shot 132 543 at $\rho_{\text{tor}} = 0.876$. Turning on $\delta B_\parallel$ also significantly increases, though not as large as the case shown in figure 4, the electrostatic heat flux $Q_{\text{es}}$ and also drives negative electromagnetic heat flux $Q_{\text{em}}$.

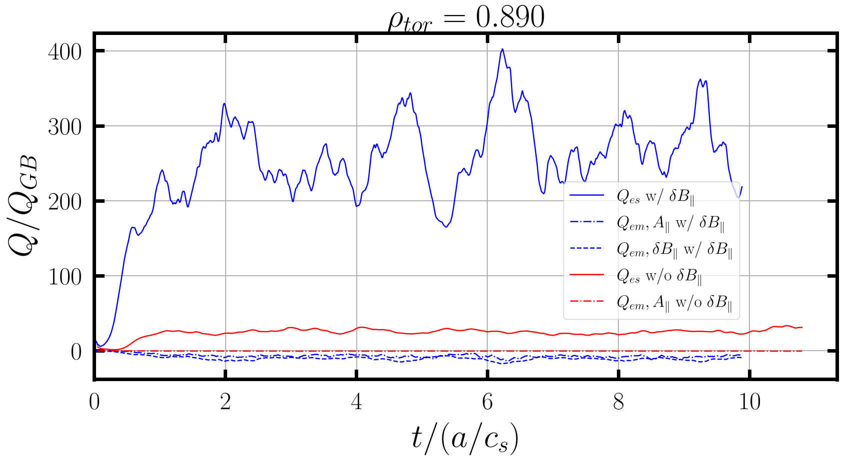

**Figure 17.** Heat flux comparisons with and without $\delta B_\parallel$ for shot 132 543 at $\rho_{\text{tor}} = 0.890$. Turning on $\delta B_\parallel$ also largely increases the electrostatic heat flux $Q_{\text{es}}$.

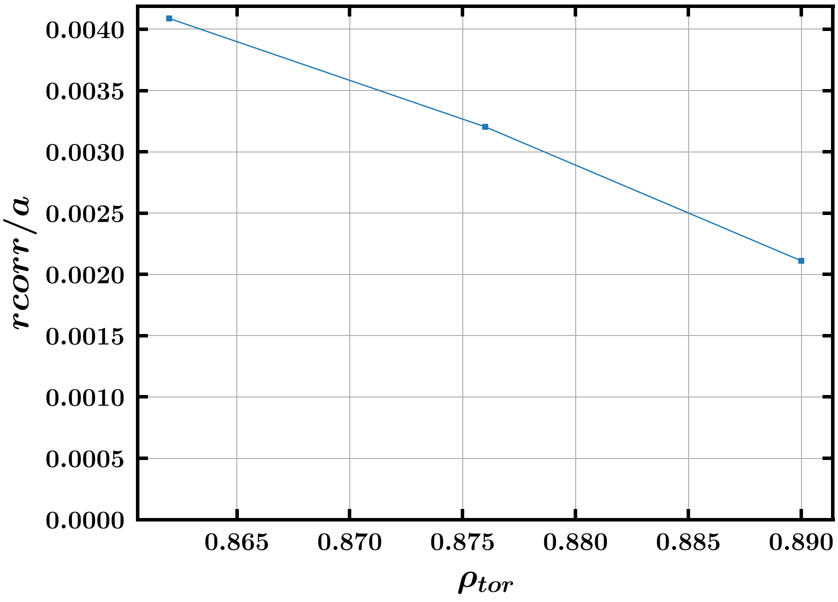

**Figure 18.** The correlation length reduces as $\rho_{\text{tor}}$ increases for shot 132 543, suggesting the fact that the instabilities are formed in the smaller radial scale or larger $k_x$.

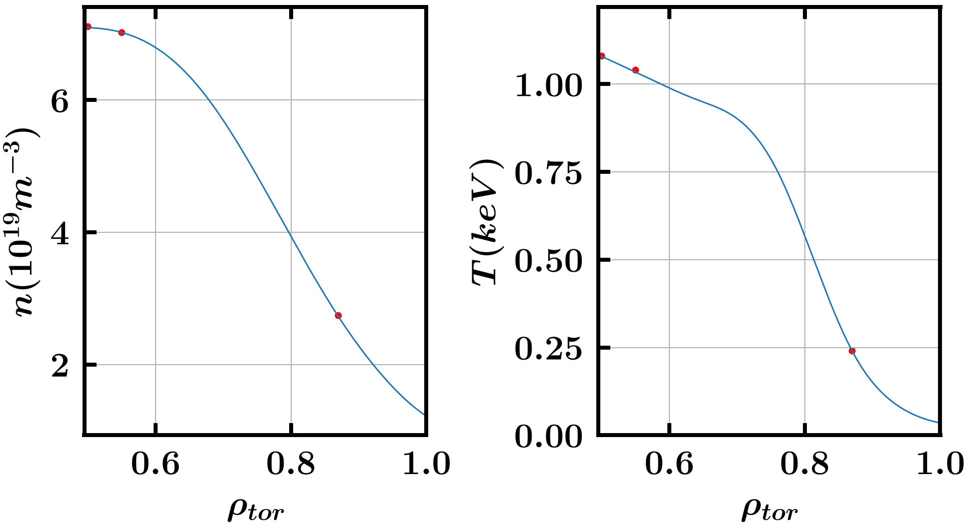

**Figure 19.** The electron density and temperature versus the square root of the normalized toroidal flux surface label $\rho_{\mathrm{tor}}$ for wide pedestal case shot 132 588.

**Table 2.** The physical input parameters for shot 132 588 at $\rho_{\mathrm{tor}} = 0.5, 0.55, 0.87$, respectively. Magnetic shear is significantly larger in the steep gradient region compared to the density pedestal top.

| $\rho_{\mathrm{tor}}$ | $q_0$ | $\hat{s}$ | $\omega_{\mathrm{ne}}$ | $\omega_{\mathrm{Te}}$ | $\eta$ | $\beta_{\mathrm{e,unit}}$ | $B_{\mathrm{unit}}(T)$ | $T_{\mathrm{e}}$(keV) | $n_{\mathrm{e}}(10^{19}\mathrm{m}^{-3})$ | $\rho^*$ |
|---|---|---|---|---|---|---|---|---|---|---|
| 0.5 | 2.91 | 0.82 | 0.066 | 0.78 | 11.8 | 2.71% | 1.067 | 1.08 | 7.11 | 0.007 53 |
| 0.55 | 3.11 | 0.80 | 0.40 | 0.90 | 2.25 | 2.37% | 1.11 | 1.04 | 7.02 | 0.007 08 |
| 0.87 | 5.95 | 5.41 | 7.61 | 20.0 | 2.63 | 0.11% | 1.56 | 0.24 | 2.74 | 0.002 44 |

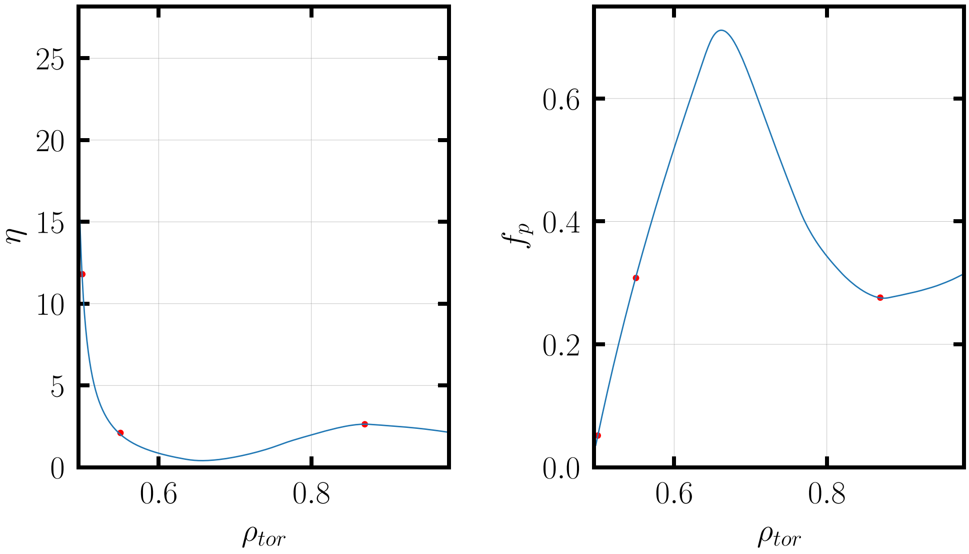

**Figure 20.** The electron density and temperature versus the square root of the normalized toroidal flux surface label $\rho_{\mathrm{tor}}$ for wide pedestal case, shot 132 588.

In addition to $\omega_*$, the substantial value of $\beta$ at the pedestal top in the wide pedestal scenario can also profoundly influence the ETG dynamics. As shown above in figure 7, ETG turbulence in NSTX demonstrates sensitivity to $\beta$, with the potential for stabilization. The value of $\beta$ at the pedestal top surpasses that in the steep gradient region by approximately a factor of twenty. This notable variation suggests that alternative electromagnetic instabilities, such as MTM and KBM, may hold greater relevance in this specific radial location, which will also be investigated in the future. Such observations imply that, unlike the narrow pedestal cofigurations, ETG turbulence is unlikely to control the evolution of the pedestal top in the wide pedestal scenarios; the impact of $\delta B_{||}$ on ETG turbulence, therefore, becomes inconsequential.

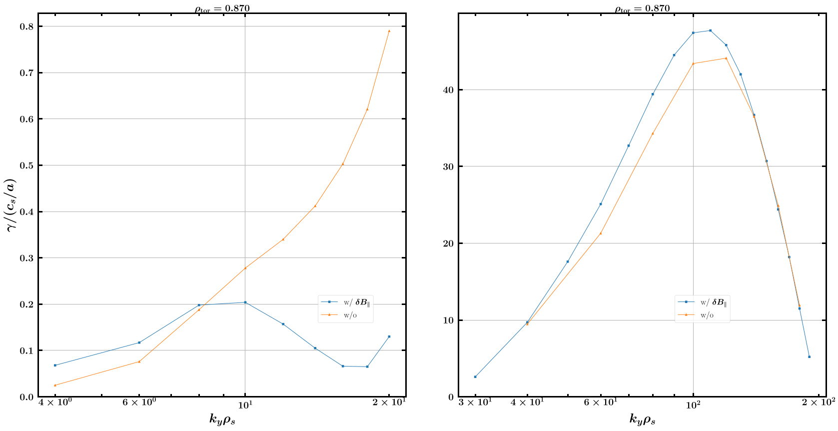

**Figure 21.** Growth rate spectrum with and without $\delta B_\parallel$ for shot 132 588 at $\rho_{\mathrm{tor}} = 0.870$ which confirms that the ETG turbulence is unstable in the steep gradient region. In contrast to the narrow pedestal case, ETG turbulence is stabilized when $\delta B_\parallel$ is turned on.

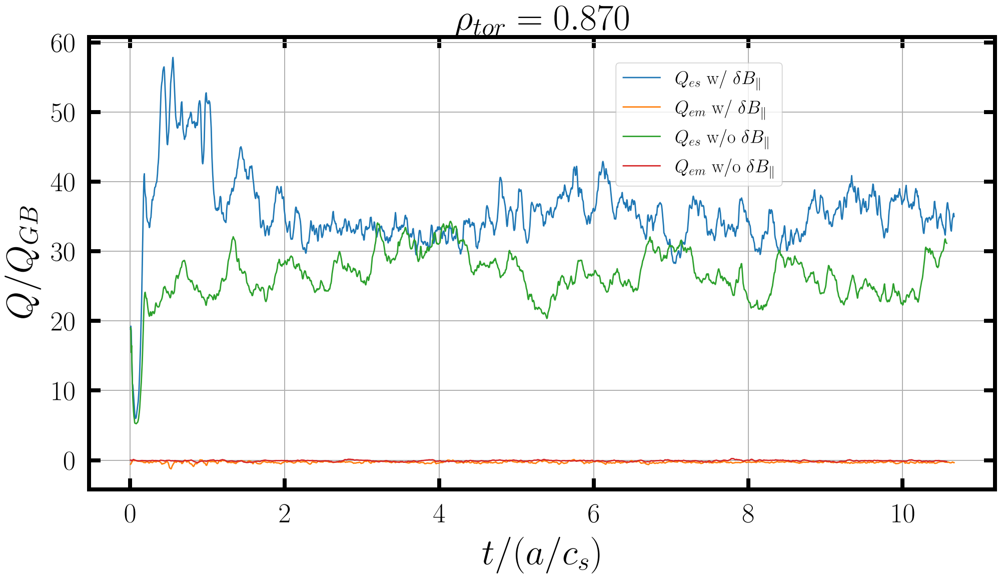

**Figure 22.** Heat flux comparison with and without $\delta B_\parallel$ shot 132 588 at $\rho_{\mathrm{tor}} = 0.870$. The heat flux is up only 20% with $\delta B_\parallel$ on, a significant departure from the pedestal top case for narrow pedestal.

Shifting our focus away from the density pedestal top towards the steep gradient region at $\rho_{\mathrm{tor}} = 0.87$, familiar patterns reemerge. As illustrated in figure 21, the growth rate spectrum indicates the presence of unstable ETG turbulence in the steep gradient region.

Unlike the narrow pedestal scenario, the unstable region in the steep gradient region extends to smaller scales, with a peak occurring around $k_y \sim 100$. This broader spectral distribution diminishes the profound effects of $\delta B_\parallel$ across most of the spectrum, except for the range between $k_y \sim 10$ and 30.

An intriguing observation from figure 21 is that, contrary to the situation in the narrow pedestal case, growth rates within the targeted range decline when $\delta B_\parallel$ is turned on. Notably, equation (10) solely determines whether $\delta B_\parallel$ can influence the electrostatic potential $\Phi$, without providing information on how it will affect ETG turbulence. Such determination necessitates knowledge about the structure of the distribution function. Hence, the contrasting behavior of $\delta B_\parallel$ in comparison to the narrow pedestal case is not surprising.

Examining the heat flux time traces depicted in figure 22, we observe a mere 20% increase in heat flux in the presence of $\delta B_\parallel$. This subtle change can be attributed to the similarity in growth rate spectra, marking a notable departure from the scenario observed in the pedestal top case for the narrow pedestal. However, a pertinent question arises: Why does the heat flux still increase despite the similarity in the growth rate spectra, especially considering that the spectrum without $\delta B_\parallel$ exhibits higher growth rates around $k_y \sim 10$ to 30?

A closer inspection of figure 23, which presents the heat flux spectrum, sheds light on this matter. The heat flux generated in the larger-scale region of the ETG turbulence spectrum is more pronounced in the absence of $\delta B_\parallel$. Conversely, when considering the heat fluxes in the smaller-scale region of the ETG turbulence spectrum, we observe that the scenario with $\delta B_\parallel$ on yields approximately twice the heat flux. Interestingly,

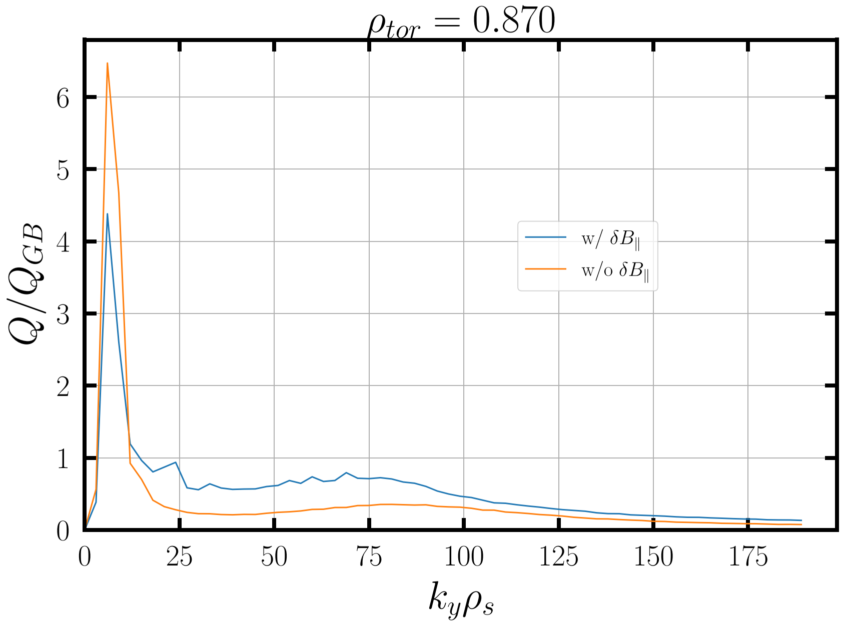

**Figure 23.** Heat flux spectrum comparison with and without $\delta B_{\|}$ for shot 132 588 at $\rho_{\rm tor} = 0.870$. With $\delta B_{\|}$ on, the large scale ETG instabilities are less active and the multiscale interactions are weaker.

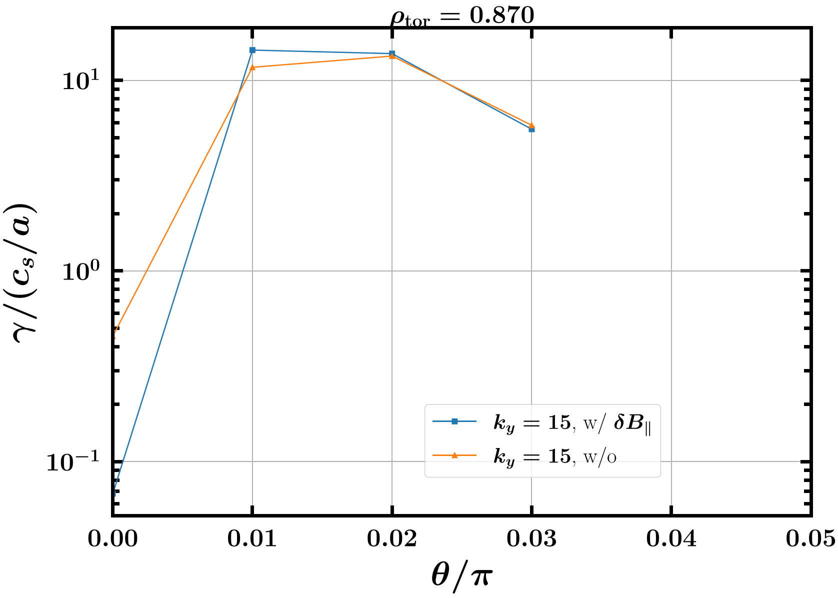

**Figure 24.** The ballooning angle scan for $k_y = 15$ for shot 132 588 at $\rho_{\rm tor} = 0.870$. The growth rate with $\theta = 0$ is stabilized by $\delta B_{\|}$.

as indicated in figure 21, the growth rates show some, but not significant, disparity at smaller scales ($\sim$10%), suggesting that linear physics can partly explain the heat flux behavior; however, the discrepancy still requires nonlinear interactions, which amplify variations in growth rates at larger scales.

To address this issue, we can look at the gyrokinetic nonlinearity of the distribution function $g_{j,k}$ at wavenumber $k$ from equation (3). Understanding how cross-scale nonlinear interactions affect turbulence levels involves dividing equation (3) into two components: $\left(k'_x k_y - k_x k'_y\right)$ and $\chi_{j,k'} g_{j,k-k'}$. The former, representing the coupling coefficient, naturally increases with larger $k$ and $k'$. Consequently, if sidebands with larger non-zero $k_x$ are more active, the nonlinearity diverting energy away from $k_x = 0$ modes becomes more efficient [47–51]. Additionally, the stronger excitation of larger-scale modes augments the magnitude of $\chi_{j,k'} g_{j,k-k'}$, leading to increased nonlinearity. Therefore, an increase in growth rates of larger-scale modes, alongside a broader growth rate spectrum versus ballooning angle for smaller-scale modes upon deactivating $\delta B_{\|}$, suggests that the smaller-scale modes in the absence of $\delta B_{\|}$ result from heightened multi-scale interactions.

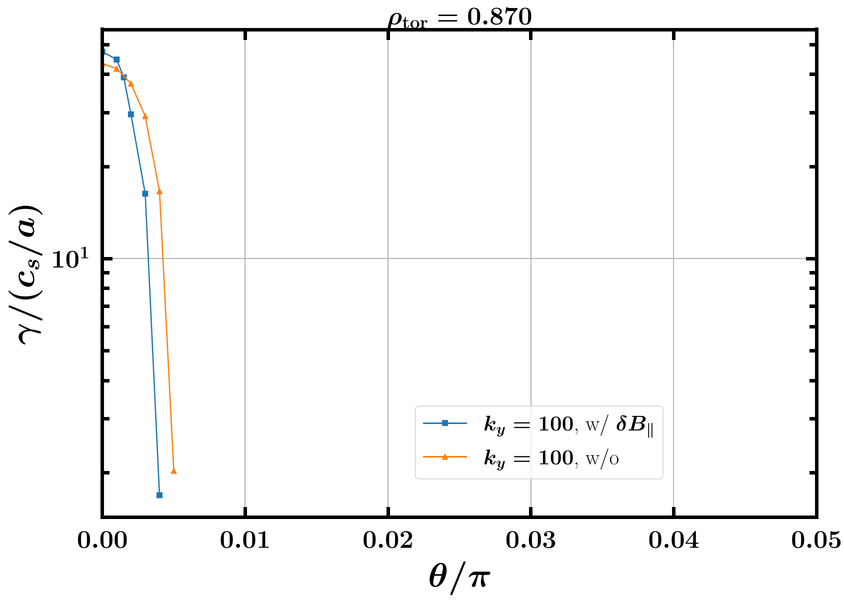

**Figure 25.** The ballooning angle scan for $k_y = 100$ for shot 132 588 at $\rho_{\rm tor} = 0.870$. The unstable region is larger with $\delta B_\|$ on.

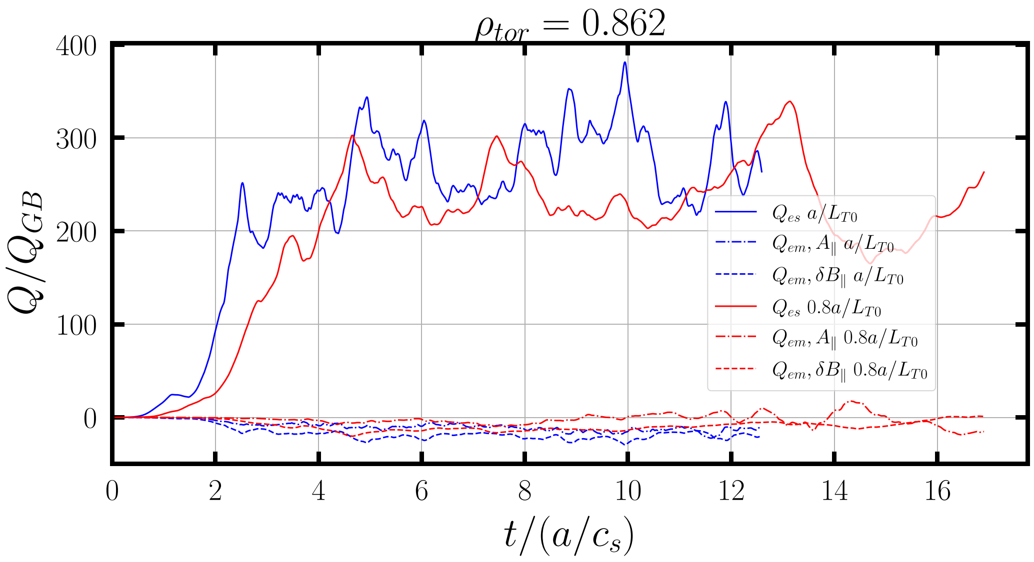

**Figure 26.** Heat flux comparison between the original parameter and the one with 20% smaller electron and ion temperature gradients for shot 132 543 at $\rho_{\rm tor} = 0.862$. The electrostatic heat flux is only reduced 10%, implying the ETG transport at this radial location is not stiff.

Figures 24 and 25 illustrate ballooning angle scans for $k_y = 15$ (large scale) and $k_y = 100$ (small scale). At $k_y = 15$, the growth rates of ETG modes are larger with $\delta B_\|$ on at low $\theta$ ($k_x$). Conversely, for ETG modes at $k_y = 100$, growth rates are decreased with the presence of $\delta B_\|$ marginally around $\theta = 0$, while simultaneously broadening the spectrum by approximately 20%. This observation aligns directly with the expectations of the analytic calculations. Thus, it is indeed cross-scale interactions that cause the heat flux to be lower when $\delta B_\|$ is inactive, indicating that $\delta B_\|$ impedes the growth of larger-scale ETG modes and reduces the effect of multi-scale interactions.

We return now to ETG transport in the non-lithiated discharge. As previously stated, the calculated heat flux from a nonlinear simulation at $\rho_{\rm tor} = 0.862$ with $\delta B_\|$ turned on is 10.6 MW, which is above the heating power. This motivates further investigation to determine what effects may reduce the transport to the experimentally expected range. The most plausible candidates are the stiffness of the transport (i.e. sensitivity to background gradients), global effects, and multi-scale interactions.

In order to test whether it is the stiffness of the transport that is responsible for the high heat flux, one can simply adjust the temperature gradient within reasonable bounds roughly representative of experimental uncertainty and see whether it brings down the heat flux enough. Figure 26 shows the comparison between the heat fluxes derived from the original parameter and the one with 20% smaller electron and ion temperature gradients. The electrostatic heat flux in fact only reduces $\sim 10\%$, which suggests the transport is not stiff at this radial location. Therefore, the overestimation of the heat flux is likely not the result of stiff transport.

Global effects and multi-scale interactions are important areas identified for future investigation. Prior work [50] demonstrated that in the MAST tokamak, local simulations closely matched global simulations within the steep gradient region but deviated significantly at the pedestal top. This discrepancy underscores the potential importance of global physics in shaping pedestal-top behavior. Given the structural and operational similarities, global effects could play a comparable role in NSTX and merit further analysis.

Another key mechanism that may explain the discrepancy between simulated and experimental heat flux levels is multi-scale interaction between ion- and electron-scale turbulence. Such interactions have the potential to suppress electron-scale transport and bring flux levels closer to experimental observations. However, the prohibitive computational cost of multi-scale simulations limits their feasibility within the scope of the present work.

Both global effects and multi-scale dynamics remain on the agenda for future studies. A deeper understanding of their contributions is critical for advancing predictive capabilities in transport modeling and for assessing the viability of these mechanisms in reactor-scale plasma scenarios.

## 4. Conclusion

This study provides an in-depth analysis of how a fuller treatment of ETG turbulence that includes magnetic perturbations (in particular, parallel magnetic field fluctuations, $\delta B_{||}$) may be of fundamental importance to understand the NSTX pedestal. Our results significantly advance pedestal physics, and provide critical new insights into electromagnetic effects on edge turbulence and transport.

Firstly, through a combination of analytical and numerical methods, we have established that retaining $\delta B_{||}$ can exert a pronounced effect on the ETG modes, particularly in regimes characterized by large radial scales at the intermediate bi-normal scale between ion and electron scales. This observation is novel given the fact that ETG is essentially an electrostatic instability and that ETG turbulence is often assumed to be largely insensitive to electromagnetic effects. The results from equations (8)–(10) collectively suggest that the increased average electron magnetic moment, $\langle \mu \rangle_e$, and the subsequent larger perpendicular currents, which induce larger $\delta B_{||}$ fluctuations, play a pivotal role in this enhanced sensitivity.

Furthermore, nonlinear electron-scale gyrokinetic simulations, which incorporate the effects of $\delta B_{||}$, demonstrate a substantial increase in heat fluxes through inclusion of $\delta B_{||}$. For the non-lithiated discharge at $\rho_{\text{tor}} = 0.862$, the calculated heat flux with $\delta B_{||}$ on reaches 10.6 MW, equivalent to 243 gyrobohm heat flux ($Q_{\text{GB}}$), in stark contrast with the mere 0.267 MW (6.16 $Q_{\text{GB}}$) observed without $\delta B_{||}$. This enormous difference highlights the crucial impact of $\delta B_{||}$ on the overall heat transport within the pedestal region. Clearly, this is an overestimate because the total heating power of the discharge is 6 MW. One, thus, concludes that while the heat flux with $\delta B_{||}$ is overestimated, the calculation without $\delta B_{||}$ predicts an unduly low electron heat flux from ETG turbulence. Notably, this electromagnetic ETG transport is active in precisely the region where earlier work has identified a gap between observed pressure gradients and the KBM limit. This work provides a plausible explanation for this observation.

In addition, our investigation reveals that both $A_{||}$ and $\delta B_{||}$ contribute negatively to $Q_{\text{em}}$, the electromagnetic heat flux; $\delta B_{||}$ contributes 50% more than $A_{||}$. The total electromagnetic heat flux in the presence of $\delta B_{||}$ is approximately 20% of the electrostatic heat flux ($Q_{\text{es}}$), a proportion far larger than in the absence of $\delta B_{||}$. This finding underscores the heightened electromagnetic effects when $\delta B_{||}$ is present (from vanishing small to $\sim 10\%$ of $\Phi$), further emphasizing the complex interplay between magnetic field fluctuations and plasma turbulence.

This paper provides fundamental insights into edge turbulent transport in spherical tokamaks and will inform the development of rigorous predictive pedestal models.

## Acknowledgments

Computing resources from Perlmutter. This work was supported by U.S. DOE Contract Nos. DE-SC0022115 and DE-FG0204ER54742. The data supporting the findings of this study is available from the authors upon reasonable request.

## Appendix. Simulation setup

Table 3 presents the resolutions utilized in various nonlinear simulations. The table includes the following parameters: $\rho_{\text{tor}}$, which represents the radial location; $n$, denoting the number of gridpoints in each dimension; and $L_x/a$, indicating the box size with unit $r/(q\hat{s})$. The subscripts used for $n$ and $L$ are as follows: $s$ for species, $x$ for the radial direction, $y$ for the bi-normal direction, $z$ for the parallel direction, $\epsilon$ for the energy, and $\xi$ for pitch angle. Moreover, $k_{y,\min}\rho_s$ represents the minimum wavenumber in the bi-normal direction. For all simulations with the same radial location, certain values remain the same and are repeatedly displayed in the table.

The resolutions used in the nonlinear simulations-specifically $n_z$, $n_\epsilon$, and $n_\xi$-are chosen based on convergence tests from linear runs, where doubling the resolution results in less than a 3% change in growth rates. The maximum poloidal wavenumber is set as $k_{y,\max} = n_{k_y} \times k_{y,\min}$, selected to span the entire unstable wavenumber range. The minimum wavenumber $k_{y,\min}$ is determined such that halving it does not

**Table 3.** Resolutions used for different nonlinear runs.

| $\rho_{\mathrm{tor}}$ | $n_x$ | $n_{k_y}$ | $n_z$ | $n_\xi$ | $n_\epsilon$ | $k_{y,\mathrm{min}}\rho_s$ | $L_x/a$ |
|---|---|---|---|---|---|---|---|
| Shot 132 543 | | | | | | | |
| 0.862 | 256 | 32 | 64 | 16 | 8 | 2 | 256 |
| 0.876 | 256 | 64 | 64 | 16 | 8 | 2 | 256 |
| 0.890 | 256 | 64 | 64 | 16 | 8 | 2 | 256 |
| Shot 132 588 | | | | | | | |
| 0.87 | 64 | 64 | 64 | 24 | 12 | 3 | 64 |

significantly alter the heat flux spectrum (with the total heat flux changing by approximately 10.

Similarly, $n_x$ and the radial domain size $L_x/a$ are selected based on convergence criteria. However, $n_x$ is additionally chosen to include a wide stable region. A large radial domain ($L_x \sim 20\rho_s$) is essential, as insufficient domain size can lead to the development of unphysically large streamers and prevent turbulence saturation. This requirement is further justified by the high magnetic shear ($\hat{s} \sim 6$), which constrains ETG modes to low-$k_x$ space, necessitating large values for both $L_x/a$ and $n_x$.

## ORCID iDs

P.-Y. Li 0000-0002-9525-4171
D.R. Hatch 0000-0002-1625-4385
J.F. Parisi 0000-0003-1328-7154
M. Lampert 0000-0002-8462-8799
E.A. Belli 0000-0001-7947-2841

## References

[1] Maingi R. *et al* 2009 *Phys. Rev. Lett.* **103** 075001
[2] Kugel H.W. *et al* 2008 *Phys. Plasmas* **15** 056118
[3] Oyama N., Isayama A., Matsunaga G., Suzuki T., Takenaga H., Sakamoto Y., Nakano T., Kamada Y. and Ide S. 2009 *Nucl. Fusion* **49** 065026
[4] Maingi R., Hubbard A.E., Meyer H., Hughes J.W., Kirk A., Maqueda R. and Terry J.L. 2011 *Nucl. Fusion* **51** 073002
[5] Guttenfelder W. *et al* 2022 *Nucl. Fusion* **62** 042023
[6] Guttenfelder W. *et al* 2022 Pedestal transport validation in NSTX and development of a general ETG pedestal transport model *APS Division of Plasma Physics Meeting* p I01. 001
[7] Jenko F., Told D., Xanthopoulos P., Merz F. and Horton L.D. 2009 *Phys. Plasmas* **16** 055901
[8] Hatch D.R., Told D., Jenko F., Doerk H., Dunne M.G., Wolfrum E., Viezzer E. and Pueschel M.J. 2015 *Nucl. Fusion* **55** 063028
[9] Hatch D.R., Kotschenreuther M., Mahajan S., Valanju P. and Liu X. 2017 *Nucl. Fusion* **57** 036020
[10] Kotschenreuther M., Hatch D.R., Mahajan S., Valanju P., Zheng L. and Liu X. 2017 *Nucl. Fusion* **57** 064001
[11] Hatch D.R. *et al* 2019 *Nucl. Fusion* **59** 086056
[12] Kotschenreuther M. *et al* 2019 *Nucl. Fusion* **59** 096001
[13] Xing Liu M.K., Hatch D.R., Mahajan S.M., Hughes J.W. and Hubbard A.E. arXiv:2005.08924
[14] Hatch D.R. *et al* 2022 *Phys. Plasmas* **29** 062501
[15] Guttenfelder W., Groebner R., Canik J., Grierson B., Belli E. and Candy J. 2021 *Nucl. Fusion* **61** 056005
[16] Chapman-Oplopoiou B. *et al* 2022 *Nucl. Fusion* **62** 086028
[17] Joffrin E. *et al* 2019 *Nucl. Fusion* **59** 112021
[18] Parisi J.F. *et al* 2022 *Nucl. Fusion* **62** 086045
[19] Field A.R., Chapman-Oplopoiou B., Connor J.W., Frassinetti L., Hatch D.R., Roach C.M. and Saarelma S. (JET Contributors) 2023 *Phil. Trans. R. Soc. A* **381** 20210228
[20] Li P.-Y. , Hatch D.R., Chapman-Oplopoiou B., Saarelma S., Roach C.M., Kotschenreuther M., Mahajan S.M. and Merlo G. 2024 *Nucl. Fusion* **64** 016040
[21] Hatch D.R. , Kotschenreuther M.T., Li P.-Y., Chapman-Oplopoiou B., Parisi J., Mahajan S.M. and Groebner R. 2024 *Nucl. Fusion* **64** 066007
[22] Walker J. and Hatch D.R. 2023 *Phys. Plasmas* **30** 082307
[23] Jenko F., Dorland W., Kotschenreuther M. and Rogers B.N. 2000 *Phys. Plasmas* **7** 1904–10
[24] Clauser C.F., Rafiq T., Parisi J., Avdeeva G., Guttenfelder W., Schuster E. and Wilson C. 2025 *Phys. Plasmas* **32** 022305
[25] Candy J., Belli E.A. and Bravenec R.V. 2016 *J. Comput. Phys.* **324** 73–93
[26] Jenko F. 2000 *Comput. Phys. Commun.* **125** 196
[27] Chowdhury J., Chen Y., Wan W., Parker S.E., Guttenfelder W. and Canik J.M. 2016 *Phys. Plasma* **23** 012513
[28] Dominski J., Guttenfelder W., Hatch D.R., Goerler T., Jenko F., Munaretto S. and Kaye S. 2024 *Phys. Plasmas* **31** 044501
[29] Parisi J.F. *et al* 2024 *Phys. Plasmas* **31** 030702
[30] Canik J.M., Guttenfelder W., Maingi R., Osborne T.H., Kubota S., Ren Y., Bell R.E., Kugel H.W., LeBlanc B.P. and Souhkanovskii V.A. 2013 *Nucl. Fusion* **53** 113016
[31] Bourdelle C. , Dorland W., Garbet X., Hammett G.W., Kotschenreuther M., Rewoldt G. and Synakowski E.J. 2003 *Phys. Plasmas* **10** 2881–7
[32] Diallo A. , Groebner R.J., Rhodes T.L., Battaglia D.J., Smith D.R., Osborne T.H., Canik J.M., Guttenfelder W. and Snyder P.B. 2015 *Phys. Plasmas* **22** 056111
[33] Pueschel M.J., Jenko F., Told D. and Büchner J. 2011 *Phys. Plasmas* **18** 112102
[34] Kotschenreuther M. , Liu X., Mahajan S.M., Hatch D.R. and Merlo G. 2024 *Nucl. Fusion* **64** 076033
[35] Candy J. 2009 *Plasma Phys. Control. Fusion* **51** 105009
[36] Waltz R.E. and Miller R.L. 1999 *Phys. Plasmas* **6** 4265
[37] Kennedy D. *et al* 2024 *Nucl. Fusion* **64** 086049
[38] Chapman-Oplopoiou B., Walker J., Hatch D.R. and Görler T. (JET contributors) 2024 *Phys. Rev. Res.* **7** L012004
[39] Stephens C.D. and Li P.-Y. 2025 arXiv:2501.00698
[40] Merz F. 2008 Gyrokinetic simulation of multimode plasma turbulence *PhD Thesis* Westphalian Wilhelms University of Münster
[41] Abel I.G., Plunk G.G., Wang E., Barnes M., Cowley S.C., Dorland W. and Schekochihin A.A. 2013 *Rep. Prog. Phys.* **76** 116201
[42] Parra F.I. and Catto P.J. 2008 *Plasma Phys. Control. Fusion* **50** 065014

[43] Frieman E.A. and Chen L. 1982 *Phys. Fluids* **25** 502–8
[44] Catto P.J., Tang W.M. and Baldwin D.E. 1981 *Plasma Phys.* **23** 639
[45] Makino R. *et al* 2013 *Plasma Fusion Res.* **8** 2402115
[46] Hassan E., Hatch D.R., Guttenfelder W., Chen Y. and Parker S. 2021 *Phys. Plasmas* **28** 062505
[47] Pueschel M.J., Li P.-Y. and Terry P.W. 2021 *Nucl. Fusion* **61** 054003
[48] Terry P.W., Li P.-Y., Pueschel M.J. and Whelan G.G. 2021 *Phys. Rev. Lett.* **126** 025004
[49] Li P.-Y., Terry P.W., Whelan G.G. and Pueschel M.J. 2021 *Phys. Plasmas* **28** 102507
[50] Li P.-Y., Pueschel M.J., Terry P.W. and Whelan G.G. 2023 *Nucl. Fusion* **63** 026028
[51] Li P.-Y. and Terry P.W. 2022 *Phys. Plasmas* **29** 042301
[52] Candy J., Belli E.A. and Staebler G. 2020 *Plasma Phys. Control. Fusion* **62** 042001